

Identifying Ice-Rafted Debris Offshore of Antarctica Using a Multi-analysis Approach

Alejandra Vega González
Charlottesville, VA

B.S. Geology, University of Puerto Rico at Mayagüez, 2023

A Thesis presented to the Graduate Faculty of the University of Virginia in Candidacy for the
Degree of Master of Science

Department of Environmental Sciences

University of Virginia
April 2025

Committee:
Lauren Miller (Advisor)
Matthew Reidenbach
Justin Richardson

Abstract

The Antarctic Ice Sheet (AIS) has undergone accelerated mass loss in recent decades, primarily driven by the intrusion of warm water masses and the thinning or collapse of ice shelves, with significant implications for global sea-level rise. However, long-term AIS variability in response to climatic forcing remains poorly constrained beyond the satellite observational record. Ice-raftered debris (IRD) preserved in marine sediment cores offers a critical proxy for reconstructing past iceberg discharge and glacial dynamics along the Antarctic margin. This study applies a multiproxy framework to identify and characterize IRD in legacy sediment cores from the Weddell Sea and George V Land continental margins. Analytical methods include laser particle size analysis (LPSA), grain shape metrics, magnetic susceptibility (MS), elemental geochemistry (XRF), and scanning electron microscopy (SEM) of quartz grain microtextures. Results reveal pronounced spatial variability in IRD deposition, with the highest abundance and variability recorded in Weddell Sea continental slope cores. These IRD-bearing intervals are characterized by poorly sorted, coarse-grained sediment enriched in Fe, Ti, and Zr, alongside elevated MS values—indicative of episodic lithogenic input from iceberg rafting and subglacial sediment delivery. In contrast, abyssal plain and George V Land cores exhibit finer-grained, more uniform sedimentation and less frequent IRD input, consistent with greater distance from grounding line sources. Statistical analyses, including correlation matrices and principal component analysis (PCA), demonstrate strong covariation among maximum grain size (D100), MS, and terrigenous elemental concentrations in IRD-bearing layers. The diagnostic power of this multiproxy approach is formalized through an IRD index (0–4), which integrates multiple independent indicators to classify IRD presence across cores. These findings underscore the complex, regionally variable nature of IRD delivery in Antarctic margin sediments and contribute a refined methodological framework for paleoenvironmental reconstructions of AIS dynamics and iceberg discharge histories in polar marine settings.

Acknowledgments

A Lauren, gracias por la gran oportunidad de trabajar contigo en este proyecto. Confiaste en mí y me diste el espacio para crecer como científica y profesional. Admiro profundamente tu generosidad como mentora y la calidad humana que te define. Ha sido un honor aprender de ti.

A Natalia, gracias a la ciencia (y a Lauren) he tenido la oportunidad de conocer el gran ser que eres, gracias por enseñarme tanto, por la compañía en el laboratorio y las risas entre tantas muestras.

A mi familia, José Luis y amistades - gracias por un apoyo incondicional. Los amo.

Dr. Richardson and Dr. Reidenbach, I am grateful for the time, thoughtful comments, and expertise each of you contributed to this project. Thank you for your guidance and support throughout this process.

Table of Contents

Introduction	5-7
Research Questions.....	7
Background and Motivation.....	8-9
Materials and Methods.....	10-14
Results.....	14-22
Discussion.....	22-29
Conclusions and Future Work.....	29-30
References.....	30-34
Appendix I.....	35-54
Appendix II.....	55-58

1. Introduction

Large portions of the Antarctic Ice Sheet (AIS), particularly those resting on terrain at elevations below sea level and in direct contact with the ocean, have experienced an accelerated rate of mass loss, contributing substantially to the global rise in sea levels (Figure 1; Shepherd et al., 2012; Rignot et al., 2019; Cazenave et al., 2018; Fox-Kemper et al., 2021). The drivers of this mass loss are complex and occur on a variety of compounding timescales, but recent studies indicate that the intrusion of warm Circumpolar Deep Water (CDW) onto the continental shelf plays a significant role in melting the undersides of floating ice shelves, the seaward extension of grounded ice sheets (Jenkins et al., 2018; Adusumilli et al., 2020). The inland-sloping subglacial terrain, resulting from millennia of glacial erosion and isostatic subsidence (Anderson, 1999), further exacerbates the subsequent thinning and retreat of grounded ice, which can lead to marine ice sheet instability or, in other words, runaway ice sheet retreat (Schoof, 2012; Favier et al., 2014). Although satellite observations have offered crucial insights into these processes (e.g., Lucchita, 1986; Riva, 2009), the variability in the response of the AIS to anthropogenic climate change remains poorly understood. Analysis of shallow ice cores indicates that, over centuries, the AIS has shown varied responses to climate change (Medley & Thomas, 2019). This underlines the necessity for a broader historical context beyond the satellite observational period, enabling a more complete understanding of how the AIS has responded to previous warming and deglacial events. Such knowledge is crucial for refining future ice sheet behavior forecasts and its potential impact on global sea-level rise (e.g., Ritz, 2015; Hill, 2024).

Despite the inherent challenges associated with exploring modern and historical records of the AIS, particular focus must be directed toward its ocean-terminating edges. The scarcity of direct observations in such areas can be attributed to severe environmental conditions and significant logistical barriers. Considering this, sediment cores extracted from the Antarctic continental shelf and slope are invaluable archives of historical environmental conditions. This marine sedimentary data helps to align current instrumental observations with long-term geological records, providing essential insights into the ice sheet's historical behavior (e.g., Etourneau et al., 2013; Campagne et al., 2016). A key proxy within these sediment cores is icrafted debris (IRD), which consists of relatively coarse-grained material transported and deposited by freely floating icebergs or, in some cases, by sea ice (Hemming, 2004). IRD serves as a valuable indicator of ocean conditions and circulation, iceberg calving rates, glacial processes, and climate shifts (Alley & MacAyeal, 1994; Grobe, 1987), even millions of years ago in Antarctica providing information on the first marine-based ice sheets during the Cenozoic (e.g., Carter et al., 2017).

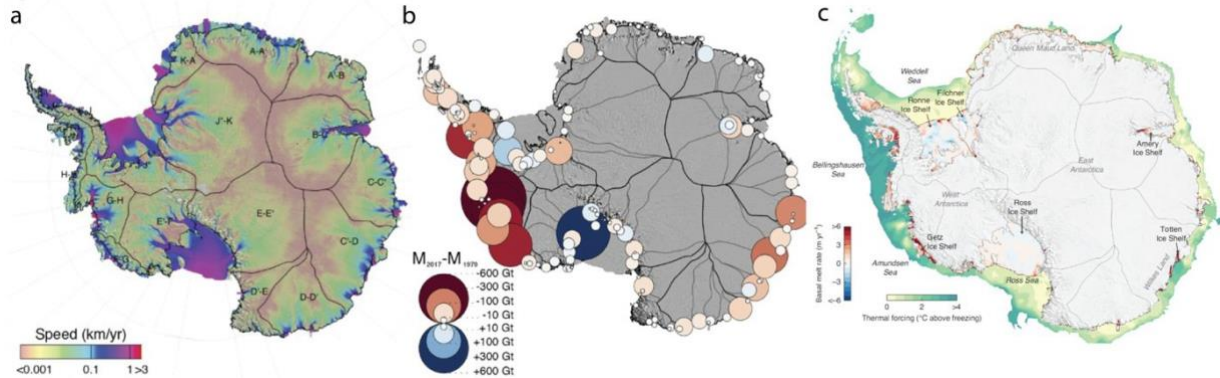


Figure 1. (a) Ice-flow speed from 2014-2016 and (b) mass loss of the AIS from 1979-2017, modified from Rignot et al. (2019). (c) Basal melt rates of ice shelves and ocean thermal forcing, modified from Adusumilli et al. (2020).

IRD, or sometimes referred to as iceberg rafted debris (IBRD), is commonly used to describe terrigenous sediment deposited in marine environments by melting icebergs, often including coarse-grained materials such as sand, gravel, and pebbles that are larger than encompassing marine sediments. However, despite its widespread application as a proxy for past glacial and marine changes, IRD remains a somewhat loosely defined concept, with its identification and interpretation varying significantly across studies and methods (McKay et al., 2022). In the high-latitude regions of the Arctic and Antarctic, the presence of coarse debris within fine-grained sediments has traditionally been linked to increased iceberg calving and icesheet instability (via the collapse of floating ice shelves), often associated with oceanic or atmospheric changes (Andrews, 2000; Grobe, 1987; Jansen et al., 2000; Kanfoush et al., 2000). Heinrich events, which occurred periodically between 70,000 and 10,000 years ago in the North Atlantic—marked by concentrated IRD layers in marine sediment cores—are interpreted as evidence of massive iceberg discharges and warming-induced collapses of the Laurentide Ice Sheet (Hemming, 2004; Andrews & Voelker, 2018). Similarly, in the Southern Ocean, IRD records are used to infer past AIS responses to climate variability (e.g., Hillenbrand et al., 2009; Passchier, 2011).

Numerous studies report enhanced IRD signals offshore Antarctica during major deglaciations, suggesting dynamic patterns of iceberg discharge and ice-sheet retreat (Patterson et al., 2014; Weber et al., 2014; Passchier, 2011; Williams et al., 2010). Yet, the processes influencing IRD deposition—ranging from iceberg calving to sediment redistribution by ocean currents—are complex and often regionally variable (Depoorter et al., 2013; Passchier, 2011). This thesis addresses these uncertainties by investigating what constitutes IRD and how it can be more reliably and holistically identified using multiple analytical techniques commonly applied to Antarctic marine sediments. Sediment cores from the Weddell Sea and George V Land (Figure 2) provide a comparative basis for exploring the spatial variability and interpretive challenges associated with IRD.

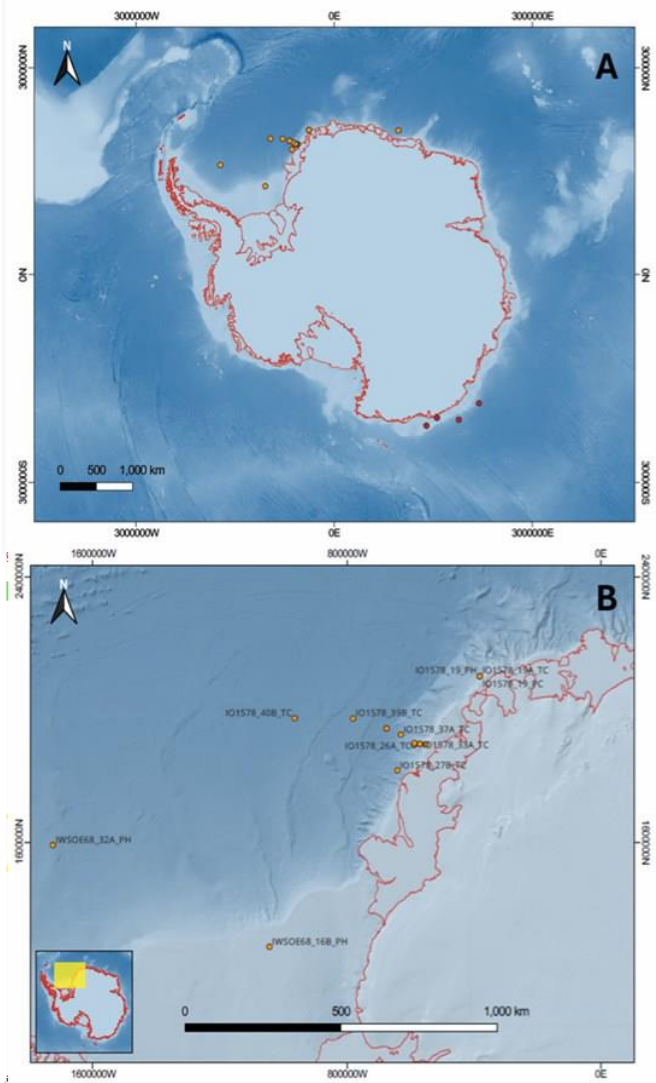


Figure 2. Locations of sediment cores sampled in this study, shown (A) across Antarctica, (B) in the Weddell Sea, and (C) in the Pennell Coast and George V Land regions. Not all cores are presented in the thesis, but analyses were conducted on all cores shown here.

2. Research Questions and Hypotheses

How does a multiproxy approach improve the identification of fine-grained IRD compared to reliance on single proxies in Antarctic margin sediments? Which sedimentological and/or geochemical variables contribute most strongly to the detection of suspected IRD in Antarctic margin cores? I hypothesize that integrating grain size and shape, bulk sediment magnetic susceptibility (MS), trace elemental composition, and scanning electron microscope (SEM) images presents a more accurate method for identifying IRD. Relying on a single technique—such as grain size or visual descriptions of clasts in cores—can overlook key grain size fractions and lead to the misinterpretation of IRD. By combining multiple analytical methods, this study provides a more comprehensive and robust framework for distinguishing IRD in marine and glacimarine sediments. I hypothesize that IRD is best identified using grain size distribution statistics (such as sorting), MS, and trace elemental concentrations derived from terrigenous material.

3. Background and Motivation

3.1 Identifying Ice-Rafted Debris in Sediment Cores.

Identifying IRD in marine sediments is essential for reconstructing past glacial dynamics and iceberg activity offshore of ice sheets, but this process requires careful distinction from other sediment sources such as gravity flows or hemipelagic input. While initial identifications often rely on visual core descriptions and counts of coarse lithic fragments, these methods alone are typically insufficient to establish an iceberg-rafted origin (e.g. McKay et al., 2022). Over time, a suite of complementary techniques has been employed to enhance IRD detection, emphasizing grain size, magnetic properties, and compositional characteristics. Grain size is one of the most widely used criteria in IRD identification. Particles exceeding 125 µm are generally considered too large to be transported long distances by ocean currents or wind, especially in deep-sea environments, and are therefore attributed to iceberg rafting (Nürnberg et al., 2011; McKay et al., 2022). However, on the Antarctic continental shelf, grain sizes > 125 µm can be found in glacial and glacial-marine sediments that have components sources from the terrestrial environment (e.g., Prothro et al., 2018). Common methods to quantify IRD include sieve-based mass percentages and laser particle size analysis (LPSA). Sieve analysis of the 250 µm to 2 mm fraction is favored for its reproducibility and compatibility with chemical pre-treatments that remove biogenic components (Patterson et al., 2014), while LPSA provides detailed grain size distributions within the 0 to 2 or 3 mm range with sub-micron to micron scale resolution, helping to characterize clay to sand fractions that may signal IRD delivery (Passchier, 2011; Hansen et al., 2015). To identify larger clasts that could potentially be IRD beyond visual inspection of sediment cores, x-radiograph (x-ray) imaging has also been widely applied in previous studies to detect >2 mm outsized clasts in sediment slabs, offering a non-destructive, downcore visual record of suspected IRD (Grobe, 1987; Cowan et al., 2008). Each method has trade-offs: sieving can be limited by sample size, LPSA can suffer from assumptions about particle properties (e.g., density, shape), and x-radiographs are sensitive to imaging conditions and operator bias; furthermore, each of these three methods focuses specifically on a certain grain size range. MS offers a valuable approach to IRD identification by detecting the concentration of magnetically susceptible minerals often originating from glacially eroded bedrock. As IRD contained in any given core likely is derived from a variety of bedrock sources, high values and variability in MS can indicate its presence (Evans and Heller, 1997). In surface sediments from the Southern Ocean, MS values have been shown to correlate with IRD concentrations, especially in iceberg-influenced areas, suggesting MS can serve as a proxy for iceberg rafting events when interpreted with care and typically alongside core lithological logs or a form of core imagery (Pirrung et al., 2002). However, MS can also be influenced by volcanic ash, authigenic minerals, glacial tills or grounding line proximal sediments, or bottom current activity (Hatfield and Stoner, 2013; Reynolds et al., 2008), which underscores the need for cross-validation by other methods. Additional insights can be gained from compositional and sub-grain scale microtextural analyses. Scanning electron microscopy (SEM) enables the identification of glacial transport indicators such as striations and conchoidal fractures on grain surfaces, providing strong evidence for subglacial

origin and iceberg rafting (Krissek, 1995; St. John et al., 2015). X-ray fluorescence (XRF) reveals changes in elemental composition that can be used to trace terrigenous input and potential shifts in sediment provenance linked to ice sheet variability (Weber et al., 2012; Ehrmann et al., 2021). Because distinguishing IRD from other sedimentary inputs requires careful interpretation, many studies have adopted a multiproxy framework to strengthen analytical confidence. Approaches that combine grain size metrics with complementary data—such as magnetic susceptibility, geochemical composition, or, in some cases, microfossil and chronological indicators—offer improved resolution and help constrain both provenance and depositional processes (Sayago-Gil et al., 2020; Knies et al., 2000). These methodological considerations provide a foundation for interpreting IRD records from the Antarctic margin, where complex depositional environments and dynamic ice sheet behavior have generated a rich archive of glacial variability. However, statistical analyses of analytical data are rarely used to quantitatively identify IRD.

3.2 Antarctic IRD Records

Studies have utilized IRD to reconstruct past ice sheet dynamics and environmental changes across the Antarctic margin and Southern Ocean. IRD records have proven valuable in identifying episodes of increased iceberg calving and assessing their links to climatic drivers. Hillenbrand et al. (2009) observed that IRD fluxes in Antarctic margin sediments often co-varied with other paleoenvironmental proxies, suggesting that large-scale climate fluctuations modulated iceberg delivery. Similarly, Kanfoush et al. (2000, 2002) identified cyclic IRD deposition from the Prydz Bay region, which was paced by Milankovitch-scale orbital variations, reinforcing the sensitivity of the East Antarctic Ice Sheet to insolation forcing. In the Weddell Sea, Ó Cofaigh et al. (2001) used IRD layers to trace repeated advances and retreats of ice streams, while Diekmann et al. (2003) documented millennial-scale IRD pulses to the Scotia Sea during the last deglaciation (20–9 thousand years ago), interpreted as reflecting episodic Antarctic Ice Sheet instability. Further insights were provided by Patterson et al. (2014), who demonstrated that IRD fluxes at IODP Site U1361, in the eastern Wilkes Land margin, tracked transitions between depositional regimes and were indicative of glacial-interglacial variability in iceberg delivery. Passchier (2011) applied LPSA to identify IRD in Pliocene sediments from Prydz Bay and emphasized the importance of grain size distributions in distinguishing iceberg transport from other depositional processes. Williams et al. (2010) and Williams & Handwerger (2005) linked high-resolution IRD records off Prydz Bay to Pliocene climate variability, revealing a strong correlation between IRD peaks and warmer Southern Ocean temperatures that drove enhanced ice sheet retreat. Weber et al. (2014) further supported the use of IRD as a deglacial proxy, finding that IRD-rich layers coincided with other signals of Antarctic ice mass loss. Additional work by Ehrmann & Grobe (1991), Hepp et al. (2006), and Hillenbrand & Fütterer (2001) highlighted the utility of IRD in tracing Antarctic contributions to abrupt climate events, such as Heinrich-like pulses in the Southern Hemisphere. Together, these studies underscore the significance of IRD as a robust proxy for interpreting past ice sheet behavior and its coupling with oceanographic and climatic systems.

4. Materials and Methods

4.1 Legacy Core Sampling and Description

This study draws on over 200 discrete samples from legacy sediment cores collected from the continental shelves and slopes of the Weddell Sea and George V Land (**Figure 2; Table 1**). These cores were acquired during major expeditions: Isla Orcadas (1978, IO1578) for the Weddell Sea, and Eltanin Expedition 37 (1969, ELT37) for George V Land. Original core descriptions—documenting lithology, grain size, and clast presence—were made aboard the research vessels, and the cores were later archived in refrigerated conditions at the NSF Antarctic Core Collection, housed at OSU-MGR.

Prior to sampling, cruise reports and original core logs were reviewed to identify samples with high potential for IRD analysis. Priority was given to cores with coarse-grained intervals and glacial-marine sedimentary features such as laminated silty clays, dropstones, outsized clasts, sharp basal contacts, color banding from meltwater pulses, and silt-rich, low-biogenic deposits typical of meltwater plumes (Prothro et al., 2018). Selected cores were subsampled at ~10-cm intervals for sedimentologic and geochemical analysis. During on-site visits to OSU-MGR, all cores were visually re-examined for clast content, sediment color, and stratigraphy. Piston cores, owing to their preservation and length, were prioritized for discrete sampling and high-resolution continuous MS scanning, conducted on-site at the repository. A summary of original core descriptions and key data (described below) plotted down core are available in **Appendix 1**.

Table 1. Core Details

Cruise	Core	Latitude	Longitude	Water depth (m)	Recovery (cm)	Geography
IO1578	19_PC	-70.54	-10.273	1339	499	Weddell Sea continental slope
IO1578	26_PC	-71.902	-17.26	2242	1135	Weddell Sea continental slope
IO1578	30_PC	-71.982	-16.21	530	145	Weddell Sea continental shelf break
IO1578	33_PC	-71.927	-16.718	1536	521	Weddell Sea continental slope
IO1578	35_PC	-71.858	-17.17	2350	1143	Weddell Sea continental slope
IO1578	38_PC	-71.237	-19.147	4301	486	Weddell Sea abyssal plain

ELT37	11_PC	-64.52	138	519.7	817	George V Land continental slope
ELT37	15_PC	-64.048	130.253	545.5	282	George V Land continental slope

4.2 Grain Size and Shape

Grain size and shape analyses are central to identifying IRD, particularly for finer components typically less than 1–2 mm in diameter, and for inferring sediment transport processes and depositional environments. LPSA was performed using a Bettersize S3 Plus, optimized for fine-grained sediments. LPSA assumes the optical and density characteristics of ideal quartz grains, which may introduce bias in natural sediments with varied compositions (McKay et al., 2022). Sediment samples (~0.5 g) were treated with a 0.05% sodium hexametaphosphate and deionized water solution to deflocculate cohesive sediments over approximately 48 hours. A magnetic stir bar homogenized the slurry, from which aliquots of grains ≤ 2 mm were pipetted into the instrument reservoir. Each run consisted of five readings to ensure reproducibility, with resulting data averaged and binned by volume percentages and cumulative volume percentages. Grain size distributions were examined for dominant peaks (as referred to as modes) in the coarse silt and sand fractions with or without finer peaks, which may reflect the co-deposition of background fine hemipelagic or glacial sediment and coarser IRD. While bimodal or multimodal distributions are not exclusive to iceberg rafting, their presence—especially when supported by other analytical indicators—was used as one line of evidence in identifying potential IRD here.

From the LPSA output, grain sizes at various percentiles of the cumulative grain size distribution were exported to calculate statistical parameters sorting (σ_1 ; Equation 1) and skewness (Sk_1 ; Equation 2) following the equations of Folk and Ward (1957).

$$\sigma_1 = \frac{\phi_{84} - \phi_{16}}{4} + \frac{\phi_{95} - \phi_5}{6.6} \quad Equation\ 1$$

$$Sk_1 = \frac{\frac{2(\phi_{16} - \phi_{84} - 2\phi_{50})}{1}}{2(\phi_{84} - \phi_{16})} + \frac{\frac{(\phi_5 - \phi_{95} - 2\phi_{50})}{2}}{2(\phi_{95} - \phi_5)} \quad Equation\ 2$$

Sorting quantifies the uniformity of grain sizes and is equivalent to the graphical standard deviation. Since our D-values represent grains that are at or below a certain grain size, rather than at or above a certain grain size, we take the absolute value (abs) of the resulting sorting values. Values <0.35 indicate very well sorted sediments; 0.35–0.50 are well sorted; 0.50–0.71 are moderately sorted; 0.71–1.00 are poorly sorted; and >1.00 are very poorly sorted. IRD-

bearing layers are often poorly to very poorly sorted due to the stochastic nature and lack of sorting mechanisms of sediment from melting icebergs. Skewness reflects the symmetry of the grain-size distribution. Positive values indicate the peak of grains skews fine (fine-skewed) with a tail in the coarser grain space, while negative values indicate a peak skewed toward coarser grains (coarse-skewed), which may suggest deposition of IRD. For reference D₅₀ is the median grain size, while D₁₀₀ is the maximum grain size of any given samples

Following grain-size analysis, shape measurements were performed on the same aliquot using the BetterSize, which captures grain photographs with the integrated microscope charge-coupled device cameras at 0.5× and 10× magnification. Out of the thousands images collected, a random subset of 200 grains was analyzed for shape descriptors—circularity and eccentricity—following methods adapted from Lepp et al. (2024). We then looked at the average values for each sample based on the 200 randomly selected grains, as well as the standard deviation (SD) of the 200 grains per sample. These shape metrics offer additional insight into sediment transport pathways and depositional energy. Circularity (C; Equation 3) quantifies how closely a particle approximates a perfect circle following:

$$C = \frac{4\pi A}{P^2} \quad \text{Equation 3}$$

where A is the area and P is the perimeter. Values closer to 1 indicate more rounded grains, often associated with prolonged or more intense transport. Lepp et al. (2024) found higher circularity in meltwater plume deposits compared to subglacial diamictons, suggesting more extensive glacial-fluvial transport. Eccentricity (E; Equation 4) measures grain elongation, calculated as:

$$E = \sqrt{(1 - (\frac{b}{a})^2)} \quad \text{Equation 4}$$

where a and b are the lengths of the major and minor axes, respectively. High eccentricity (approaching 1) reflects elongated shapes, often characteristic of minimally transported or mechanically fractured grains.

Grain shape analysis has been applied in multiple glaciomarine studies. For example, Dunhill (1998) and Andrews (2000) utilized shape descriptors and surface characteristics to identify ice-rafted and sea-ice-rafted grains in high-latitude sediments, demonstrating that shape metrics can effectively differentiate depositional settings and sediment sources. These applications reinforce the value of integrating grain size and shape measurements to more precisely characterize IRD-bearing sediments and reconstruct paleoenvironmental conditions with greater confidence.

4.3 Scanning Electron Microscopy (SEM)

A subset of samples was selected for SEM based on a combination of grain size distribution patterns and original core descriptions from the research vessel, concentrating on intervals identified as relatively coarse- or fine-grained within the suspected IRD fraction and suspected

non-IRD fractions. The minimum number of images per sample is 12 and the maximum 37 with an average of 20, some images of which contain multiple grains in the image frame. The goal was to assess representative grain surface microtextures associated with glacial transport mechanisms. Prior to imaging, the dry sample was sieved through a 250- μm mesh and retained on a 63- μm sieve. The dried fraction was mounted on carbon adhesive tabs attached to aluminum stubs. Imaging was performed using an FEI Quanta 650 SEM in high-vacuum mode. Before imaging, grains were confirmed to be primarily quartz using the Oxford AZtec Energy Dispersive X-ray Spectroscopy (EDS) system. For each sample, at least 14 images were collected containing one or multiple grains. Microtexture analysis followed the criteria outlined in Lepp et al. (2024), with comparisons to established protocols (e.g., Krissek, 1995; St. John et al., 2015; Passchier et al., 2021), focusing on features such as striations, conchoidal fractures, chatter marks, and edge rounding. These microtextures were used to infer glacial transport pathways, enabling a more direct assessment of sediment provenance and IRD transport mechanisms.

4.4 Magnetic Susceptibility (MS)

MS was measured using the GEOTEK XZ system at OSU-MGR, equipped with a Bartington MS2E point sensor, producing 1-cm resolution data along the split core surface. Measurements were conducted on undisturbed, wet cores to preserve stratigraphic continuity. MS values are reported in 10^{-5} SI units, reflecting the volume-specific susceptibility of the sediment. These values capture changes in the concentration and composition of magnetic minerals, which are commonly linked to terrigenous input. Glacial-period sediments often exhibit elevated MS values in glaciomarine settings due to increased deposition of magnetically susceptible material from subglacial erosion (Pudsey and Howe, 1998; Hillenbrand et al., 2009). This study used MS data to infer shifts in sediment provenance and depositional regimes across glacial cycles (Weber et al., 2012). MS profiles were evaluated in conjunction with grain size and XRF data to aid in the identification of IRD-bearing intervals.

4.5 X-Ray Fluorescence (XRF)

XRF is widely applied in glaciomarine sediment studies for its ability to rapidly characterize elemental trends that serve as proxies for terrigenous input, marine productivity, and depositional processes (Rothwell & Croudace, 2015; Kuhn et al., 2017). Samples that were previously processed for LPSA were dried, powdered with a Retsch PM100 planetary ball mill, and sieved through a 125- μm mesh. The powdered samples were analyzed using a ThermoFisher Scientific Niton XL5 handheld XRF analyzer. Although handheld XRF devices generally have lower precision than benchtop instruments (Dunnington et al., 2019; Hahn et al., 2019), this method facilitated practical downcore comparisons of elemental concentrations in a field-accessible format (Lepp et al., 2022). The instrument was calibrated using a NIST 2709 soil standard before measurement run sessions. Two replicate runs were conducted on a random subset of samples to assess instrument precision and data consistency. Elemental concentrations (ppm) were derived from the average of three energy spectra filters using a 90-second sampling window per filter. Replicates yielded consistent results within a mean two-sigma error of $\pm 0.6\%$.

(range: $\pm 0.2\%$ to $\pm 1.6\%$) of the measurement value, indicating acceptable reproducibility for the elements of interest.

Focus was placed on elements commonly used to infer sediment provenance and depositional shifts: K, Ti, and Fe are often associated with glacially derived lithogenic input; Ca can indicate marine biogenic input or carbonate content; and Zr, frequently linked to heavy minerals, serves as a grain-size proxy (Pruysers et al., 1991; Ziegler et al., 2008; Rothwell, 2015; Hawkings et al., 2020). Elemental profiles of Ca, K, Fe, Ti, and Zr were examined downcore to identify intervals of enhanced terrigenous input or coarse-grained sediment delivery indicative of potential IRD deposition. Specifically, enrichments in Fe, Ti, and K were interpreted as increased input of glacially derived lithogenic material, while elevated Zr values were used to highlight potential coarser fractions associated with ice-raftered debris. Conversely, low Ca concentrations were considered to reflect reduced biogenic input and possible dilution by terrigenous material during IRD deposition. These elemental signals were used in conjunction with other analyses to strengthen interpretations of IRD-rich intervals.

5. Results

5.1 Grain Size and Shape

Grain size distributions for all piston cores are shown in **Figure 3**, where darkest blue color is the upper samples of the cores and the lightest cream color is the deepest sample. Cores from the Weddell Sea continental slope and shelf break (IO1578_19_PC, IO1578_26_PC, IO1578_30_PC, IO1578_33_PC, IO1578_35_PC; **Figure 2B**) exhibit a consistent fine-grained mode, with repeated secondary peaks in the coarse silt to fine sand fractions suggesting the possible presence of IRD, as the deposition of coarse material on the continental slope, where background sediments are generally finer clay and silt, can come from IRD and other glacial sources. The frequency and magnitude of coarse silt and sand peaks vary between cores, with cores IO1578_19_PC, IO1578_26_PC, and IO1578_35_PC containing the highest abundance of coarse material, including grains exceeding 100 μm in multiple depth intervals. In these cores, these coarse-grained layers appear irregularly downcore and often display relatively well-sorted coarse peaks, characteristics consistent with event-style deposition likely associated with episodic iceberg rafting events. IO1578_30_PC and IO1578_33_PC contain fewer and smaller coarse silt and fine sand peaks, with grain size distributions dominated by fine silt and clay, and limited occurrence of outsized grains. The abyssal plain core (IO1578_38_PC; **Figure 2B**) records the lowest frequency and abundance of coarse silt and fine sand. Grain size distributions in this core are predominantly unimodal, with fine-grained sedimentation throughout, interrupted only by isolated, low-amplitude coarse peaks in the upper portion of core. Grains exceeding 100 μm are rare and restricted to discrete layers. Cores from the continental slope of George V Land (ELT37_11_PC, ELT37_15_PC; **Figure 2C**) are similarly dominated by fine-grained sediment, with consistent secondary peaks in the coarse silt and fine

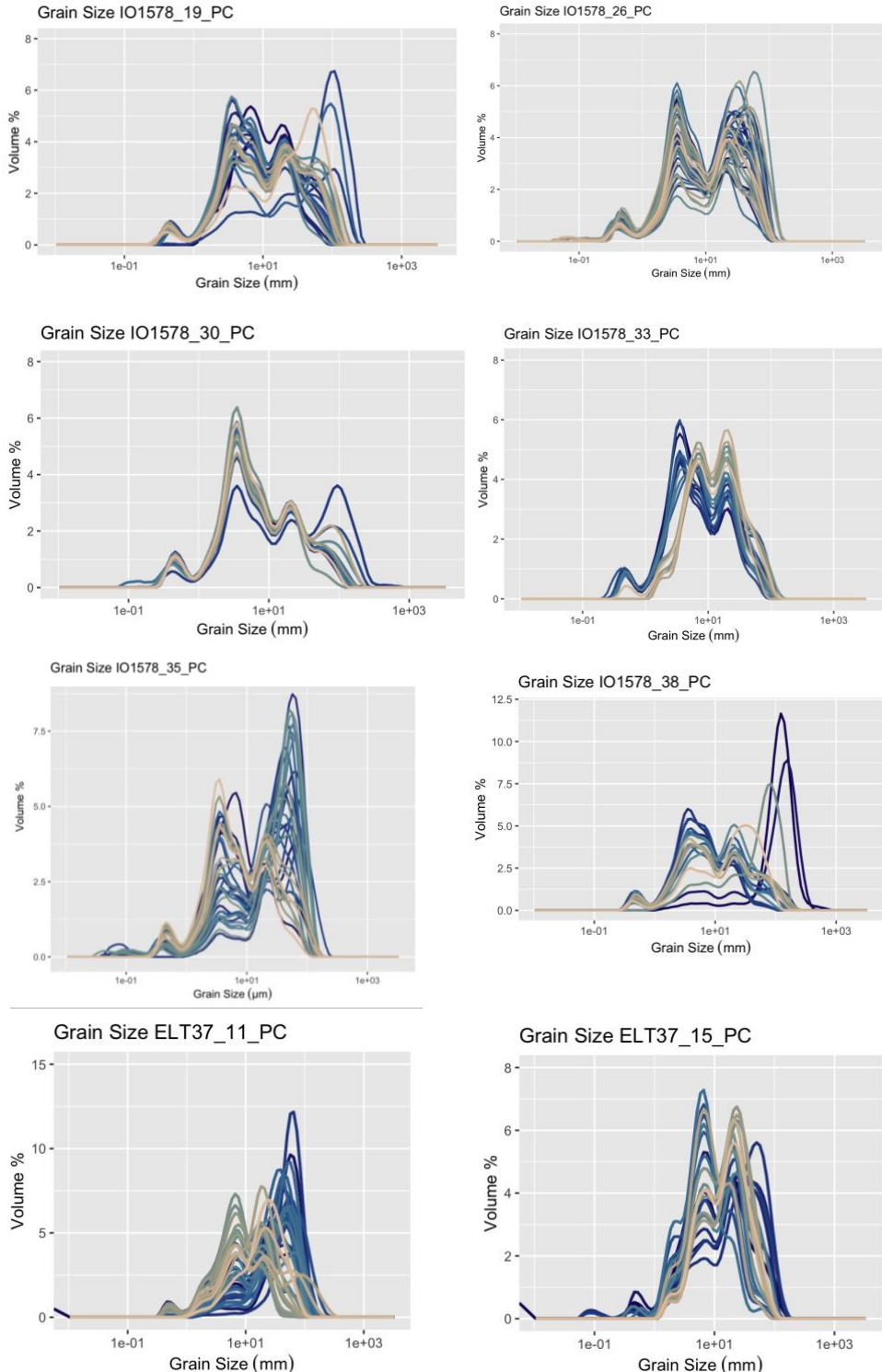


Figure 3. Grain size distributions for Weddell Sea and George V Land piston cores. Weddell Sea cores IO1578_19_PC, IO1578_30_PC, and IO1578_35_PC are characterized by multimodal patterns with dominant modes between 10–100 μm with variable coarser fractions. Weddell Sea core IO1578_26_PC exhibits high variability in coarse modes consistent with enhanced event-style coarser deposition. Weddell Sea core IO1578_38_PC is predominantly fine-grained, with isolated coarse modes. IO1578_33_PC shows lower variability in coarse fractions relative to others. George V Land continental slope cores ELT37_11_PC and ELT37_15_PC display dominant fine-grained modes (10–100 μm) with isolated coarser fractions.

sand fraction attributed. Compared to the Weddell Sea slope cores, the George V Land cores contain fewer outsized grains and lower-amplitude coarse peaks. Grains $> 100 \mu\text{m}$ are present but occur sporadically and do not dominate the grain size distributions. Grain size variability increases with depth, with deeper sections containing more frequent coarser sediment intervals relative to the upper portions of the cores.

Overall, sorting or the uniformity of grain sizes within a distribution is low, with values that are predominantly over 1 (**Appendix 2**), signifying very poorly sorted – a property common of glacially-influenced sedimentation around Antarctica and other glaciated continental margins worldwide. Skewness, a measure of toward which direction (finer or coarser) grain size distributions are skewed, aids in understanding the dominant grain sizes within a distribution. Skewness is negative for 62% of the dataset, indicating the grain size distributions tend toward the coarse endmember with all cores (except for IO1578_30_PC which only contains positive values) displaying both negative and positive values (**Appendix 2**). Notably, skewness becomes more negative as the modal grain size increases, suggesting that coarser peaks often coincide with fine-skewed distributions typical of IRD-bearing intervals. Mean eccentricity, how elliptical grains are, for each sample varies surprisingly little amongst the cores with an overall mean of 0.415 (standard deviation of 0.041; **Appendix 2**). This indicates that grains are moderately elongate. Mean circularity, another measure of grain form, for the full dataset does not vary significantly with an overall mean 0.641 (standard deviation of 0.012), indicating grains are slightly rounder than irregular in form (**Appendix 2**).

5.2 Scanning Electron Microscopy (SEM)

Quartz grain surface textures observed in SEM images display a predominance of glacial crushing features consistent with subglacial transport and deposition across the majority of analyzed intervals (**Figure 4, Table 2**). Grains from IO1578_26_PC at 90 cm, 180 cm, 340 cm, 530 cm, 770 cm, and 830 cm were largely characterized as Type C (fresh glacial crushing) following Passchier et al. (2021), based on the abundance of angular to subangular shapes, high relief, and the presence of well-developed steps, striations, and planar fracture faces. These characteristics indicate minimal post-depositional reworking and suggest direct iceberg rafting or ice-proximal sedimentation. A subset of grains, particularly at 180 cm, 340 cm, 530 cm, and 830 cm, exhibited Type D (glacial with transport modification) or Type E (glaciofluvial/littoral) characteristics, reflecting minor edge rounding, surface irregularities, or smoothing consistent with subaqueous transport or limited glaciomarine reworking. One grain from 530 cm depth was classified as Type I (periglacial chemical modification) due to the presence of irregular surface textures interpreted as silica precipitation and surface overgrowths. The relative abundance of Type C grains across depths supports a dominant subglacial transport mechanism, with localized evidence for minor transport modification within the suspected IRD fraction. These results are consistent with iceberg rafting as the primary delivery mechanism for coarser-grained sediment on the Weddell Sea continental slope. Notably, some imaged grains from IO1578_26_PC 340

cm and 830 cm, those with the lowest coarse silt/fine sand peaks, contain the most evidence of edge rounding and thus enhanced transport alteration.

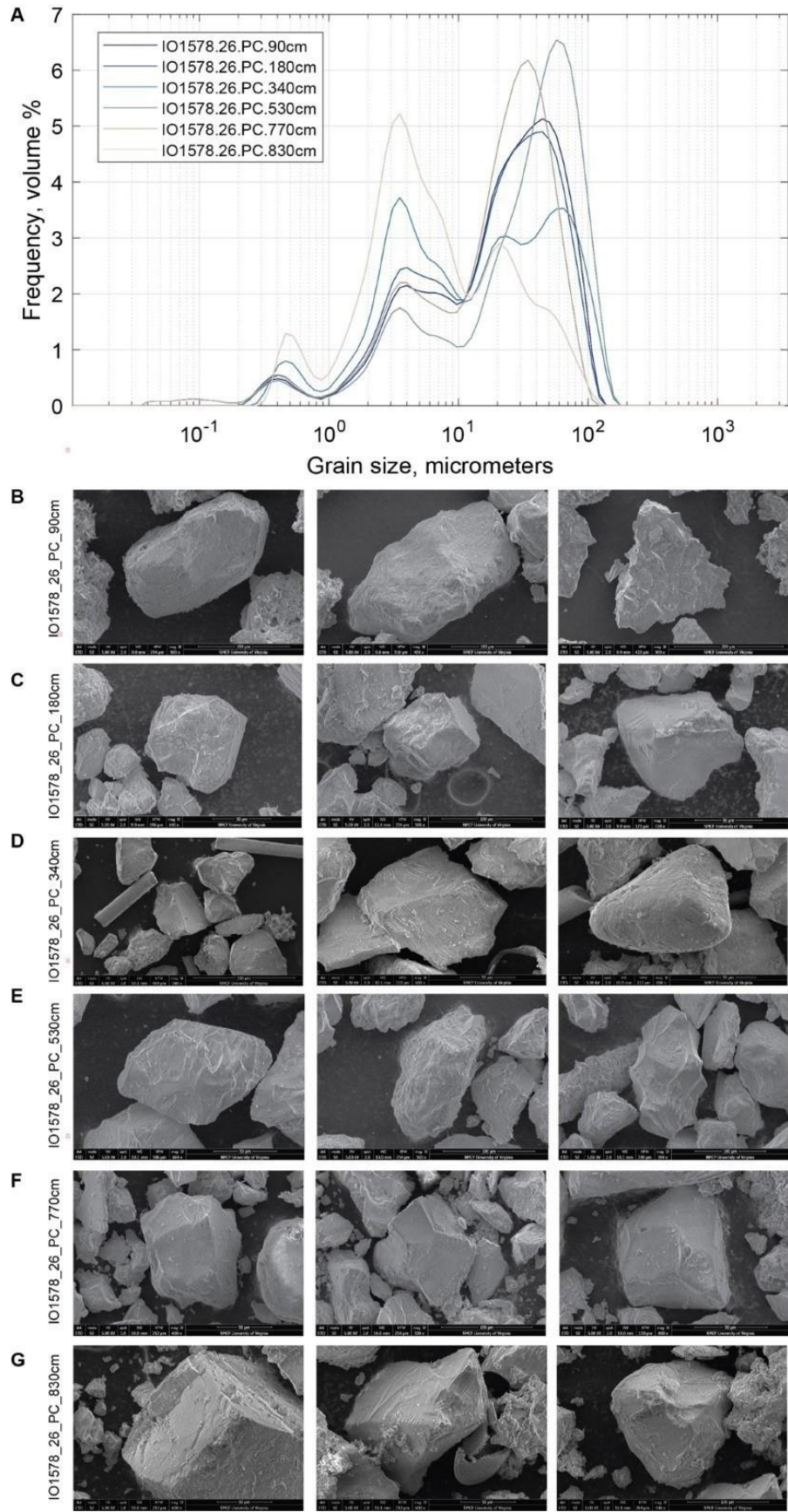


Figure 4. (A) Grain size distribution and (B) representative SEM images of quartz grains from selected depths in core IO1578_26_PC.

Table 2. SEM microtextures of images presented in Figure #. Type C = , D= , E= , I = . Gsize = grain size, MS = magnetic susceptibility, XRF = x-ray fluorescense.

Sample	Type	Edge roundness	Relief	Textures	Interpretation	IRD index
IO1578_26_PC_90cm, D B-left		Subangular to subrounded	Medium	Fractures, minor edge rounding	Glacial origin; limited reworking; lower relief suggests possible transport distance or grain size effect	1 (Gsize)
IO1578_26_PC_90cm, E B-center		Subangular to subrounded	Medium to low	Smoothed surface, irregular roughness, lack of fractures	Glacioluvial or glaciomarine reworking: abrasion and/or chemical modification	1 (Gsize)
IO1578_26_PC_90cm, C B-right		Angular	High	Steps, planar fractures, sharp edges, microblocks	Fresh glacial crushing; direct subglacial origin; minimal transport or reworking	1 (Gsize)
IO1578_26_PC_180cm D , C-left		Subangular to subrounded	Medium to High	Steps, planar fractures, minor edge rounding	Glacial origin with reworking by subaqueous transport; glaciomarine setting	1 (Gsize)
IO1578_26_PC_180cm D , C-center		Subangular to Subrounded	Medium	Planar fractures, minor steps, edge rounding, irregular surfaces	Glacial origin with reworking by meltwater or glaciomarine transport	1 (Gsize)
IO1578_26_PC_180cm C , C-right		Angular to subangular	High	Planar fractures, minor steps, edge rounding, irregular surfaces	Glacial origin with reworking by meltwater or glaciomarine transport	1 (Gsize)
IO1578_26_PC_340cm C , D-left		Angular	High	Steps, planar fracture faces, striations, sharp edges	Subglacial crushing; ice-proximal deposition; minimal reworking	2 (Gsize, XRF)
IO1578_26_PC_340cm C , D-center		Subangular	Medium to High	Striations, planar fracture faces, no rounding	Subglacial crushing; ice-proximal deposition; minimal reworking	2 (Gsize, XRF)
IO1578_26_PC_340cm E , D-right		Subrounded	Medium to Low	Smoothed surface, edge rounding	Glacioluvial or glaciomarine reworking: significant transport	2 (Gsize, XRF)
IO1578_26_PC_530cm C , E-left		Subangular	High	Steps, planar fractures, conchoidal fractures, sharp edges	Subglacial crushing; ice-proximal deposition; minimal transport or reworking	2 (Gsize, MS)
IO1578_26_PC_530cm I , E-center		Subangular to subrounded	Medium	Irregular surfaces, silica precipitation, lack of fractures	Chemical weathering and/or silica overgrowth	2 (Gsize, MS)
IO1578_26_PC_530cm C , E-right		Angular to subangular	High	Steps, planar fractures, sharp edges	Subglacial crushing; ice-proximal deposition; minimal transport or reworking	2 (Gsize, MS)
IO1578_26_PC_770cm C , F-left		Angular to subangular	High	Steps, planar fractures, sharp edges	Subglacial crushing; ice-proximal deposition; minimal transport or reworking	2 (Gsize, XRF)
IO1578_26_PC_770cm C , F-center		Angular to subangular	High	Steps, planar fractures, conchoidal fractures, sharp edges	Subglacial crushing; ice-proximal deposition; minimal transport or reworking	2 (Gsize, XRF)
IO1578_26_PC_770cm C , F-right		Subangular	Medium to High	Steps, striations, planar fractures, sharp edges	Subglacial crushing; ice-proximal deposition; minimal reworking	2 (Gsize, XRF)
IO1578_26_PC_830cm C , G-left		Angular to subangular	High	Steps, planar fractures, sharp edges, striations	Subglacial crushing; ice-proximal deposition; minimal transport or reworking	2 (Gsize, XRF)
IO1578_26_PC_830cm C , G-center		Angular	High	Steps, striations, planar fractures, sharp edges	Subglacial crushing; ice-proximal deposition; minimal transport or reworking	2 (Gsize, XRF)
IO1578_26_PC_830cm D , G-right		Subangular to subrounded	Medium	Planar fractures, surface irregularity, minor edge rounding	Glacial origin with transport modification in a glaciomarine setting	2 (Gsize, XRF)

5.3 X-Ray Fluorescence

In the Weddell Sea continental shelf and slope cores (IO1578_19_PC, IO1578_26_PC, IO1578_30_PC, IO1578_33_PC, IO1578_35_PC), Fe, Ti, and K concentrations fluctuate throughout the cores, with multiple peaks and intervals of lower background values. Zr concentrations show a similar pattern of variability, with peaks occurring at several depths (**Figure 5**). IO1578_26_PC and IO1578_35_PC exhibit the highest amplitude variability in Fe, Ti, and Zr, with frequent and sharp peaks downcore. Ca concentrations in these cores generally show less variability but decrease in certain intervals relative to the rest of the elemental concentrations. IO1578_30_PC and IO1578_33_PC display lower Fe, Ti, and Zr concentrations compared to the rest of the slope cores, with fewer distinct peaks (**Figure 5**). Ca concentrations remain relatively stable throughout these cores. In IO1578_38_PC, recovered from the Weddell Sea abyssal plain, Fe, Ti, and Zr concentrations are low and exhibit minimal downcore variability. Ca concentrations are higher and more stable relative to the slope cores, suggesting of more biogenic contributions to overall sediment accumulation. Cores from George V land (ELT37_11_PC and ELT37_15_PC) are characterized by consistently low concentrations of Fe, Ti, and Zr, with limited downcore variation (**Figure 5**). Ca concentrations are elevated in the upper portions of both cores and decrease downcore. K concentrations vary downcore in both cores, with moderate amplitude changes and isolated peaks.

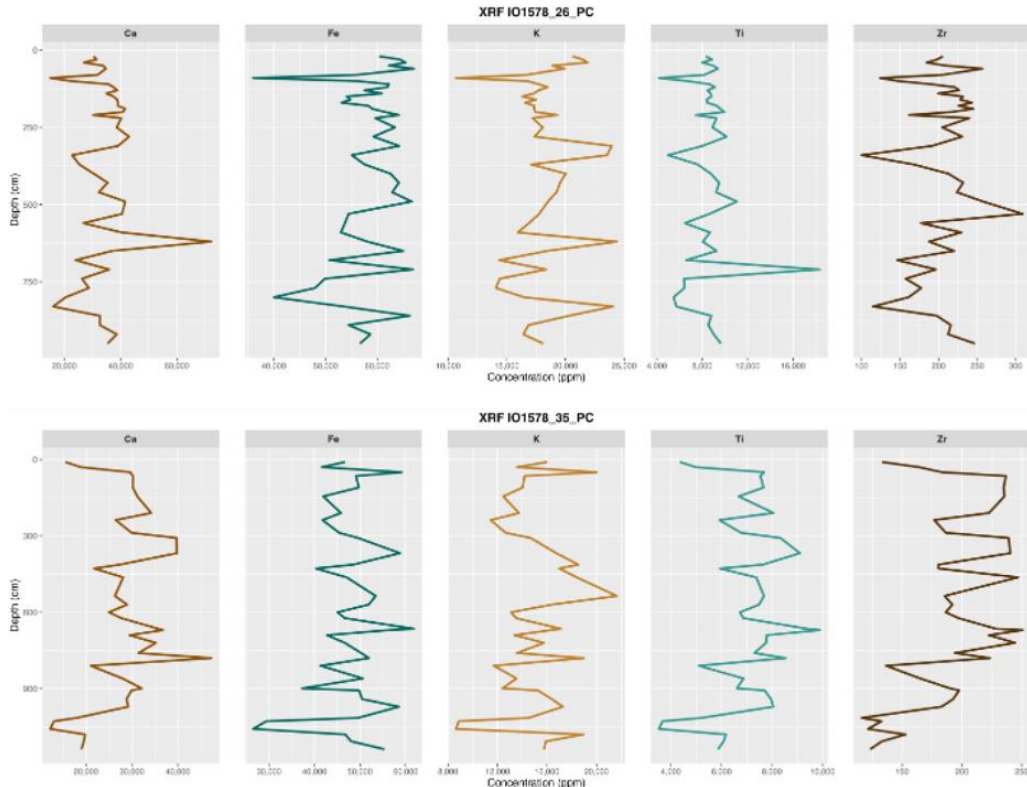


Figure 5. Downcore trace elemental concentrations for all piston cores, showing the trends and excursions in Ca, Fe, K, Ti, and Zr.

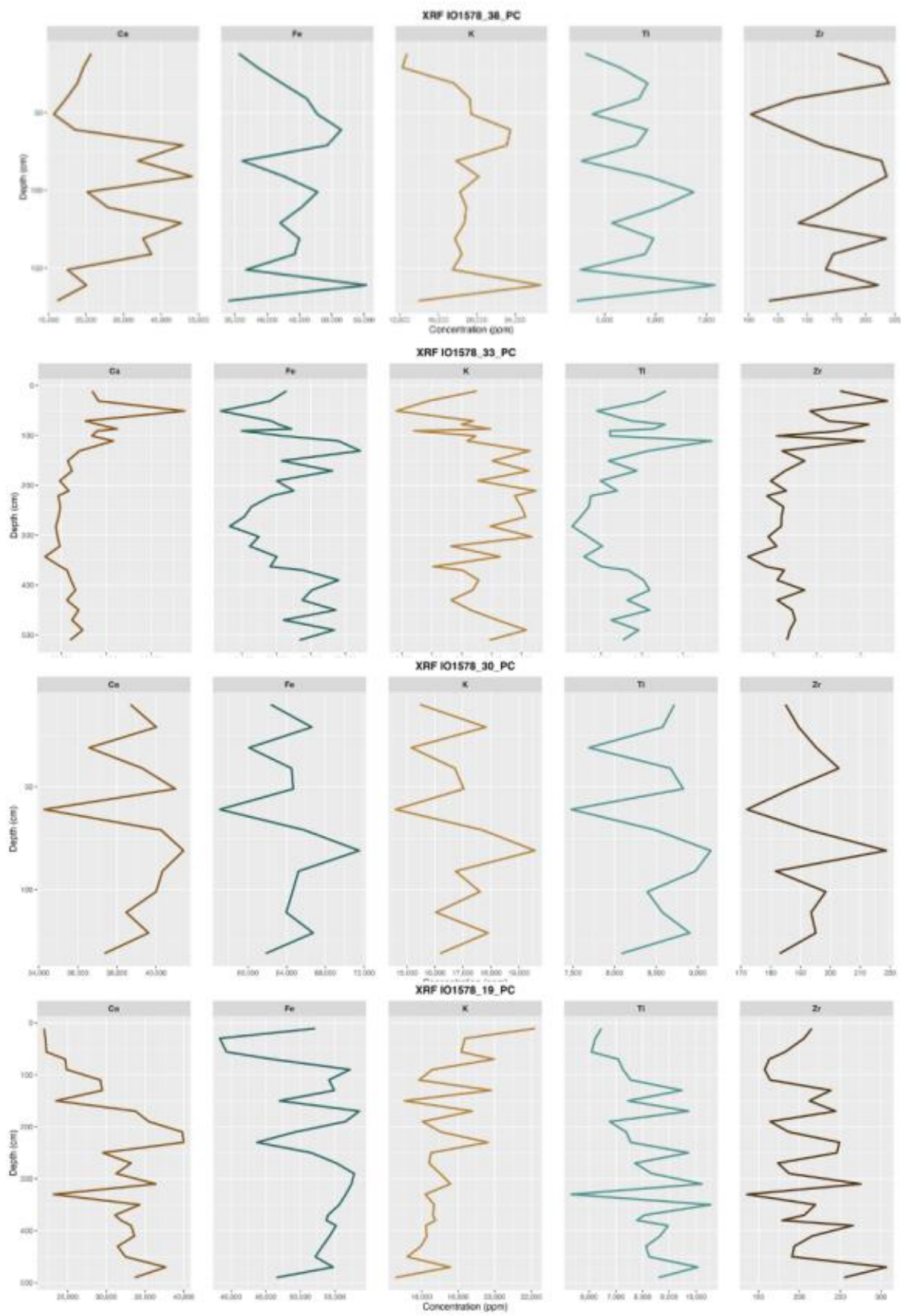


Figure 5 continued.

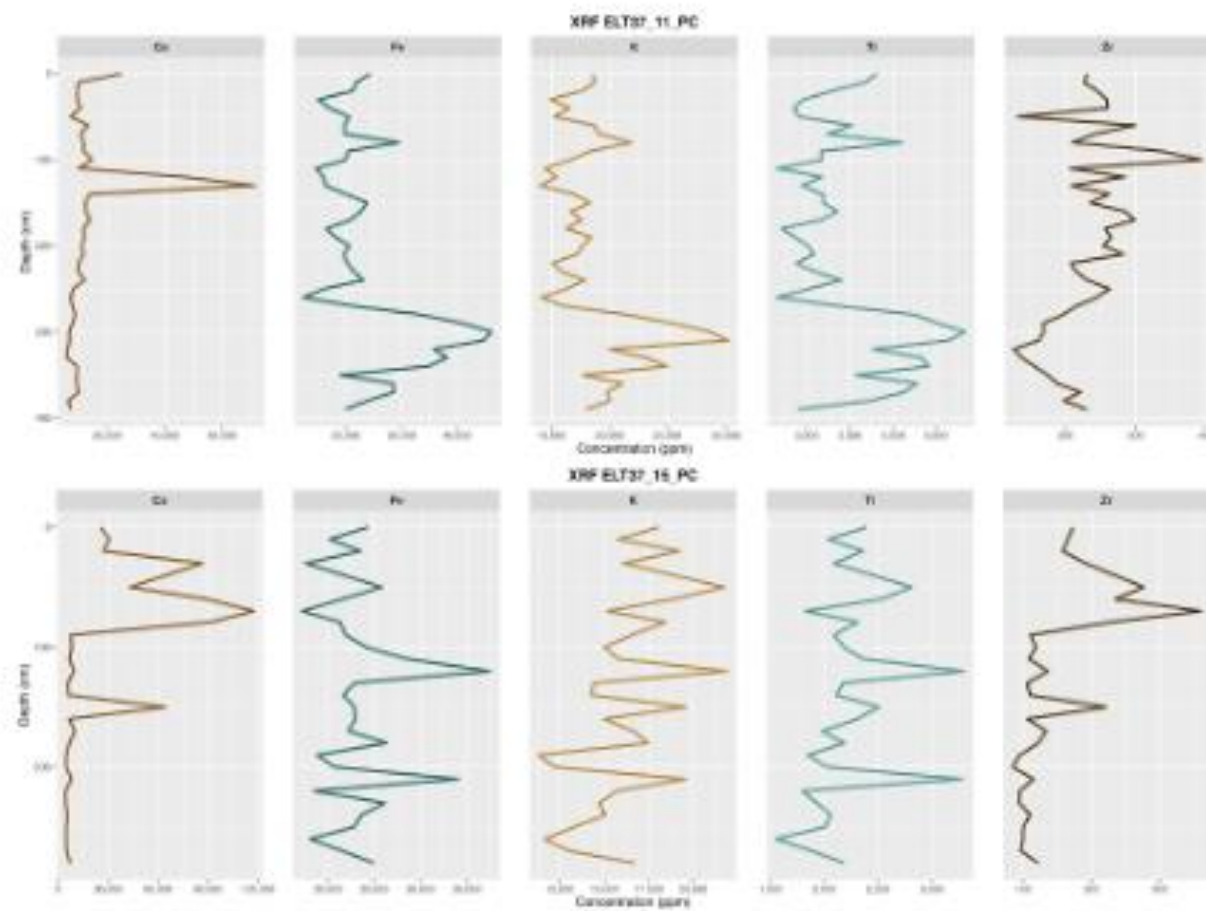


Figure 5 continued.

5.4 Magnetic Susceptibility

Cores from the Weddell Sea continental slope and shelf (IO1578_19_PC, IO1578_26_PC, IO1578_30_PC, IO1578_33_PC, IO1578_35_PC) exhibit the highest overall and greatest downcore variability in MS values (Figure 6). MS values in IO1578_19_PC and IO1578_26_PC fluctuate markedly downcore, with numerous sharp peaks reaching values between $\sim 200\text{--}400 \times 10^{-5}$ SI. These peaks correspond to intervals of increased coarse-grained material observed in the grain size distributions (Figure 3) and likely reflect enhanced terrigenous input, consistent with IRD. IO1578_26_PC, the longest of the slope cores, shows persistent variability throughout its ~ 1100 cm length, with high MS intervals interspersed with lower background values. IO1578_30_PC and IO1578_33_PC exhibit lower overall MS values relative to other slope cores, with fewer and less pronounced peaks. In IO1578_30_PC, MS values are highest in the upper ~ 200 cm, after which they decrease and remain relatively low and stable. IO1578_33_PC shows moderate downcore variability, but peak MS values are generally lower ($\sim 200\text{--}300 \times 10^{-5}$ SI) than those observed in IO1578_19_PC or IO1578_26_PC. IO1578_35_PC is notable for its sustained high MS values from ~ 300 cm to the base of the core.

(~1140 cm). This interval is marked by both elevated MS values (commonly exceeding 400×10^{-5} SI) and frequent peaks, suggesting prolonged intervals of increased lithogenic input, possibly linked to persistent IRD deposition or proximity to sediment sources. The abyssal plain core, IO1578_38_PC, displays consistently low MS values ($<200 \times 10^{-5}$ SI) throughout, with minimal downcore variability. The MS profile is relatively stable, with only minor peaks in the upper ~100 cm, coinciding with the limited coarse-grained material observed in grain size distributions (Figure 3). This suggests a dominance of fine-grained background sedimentation with occasional, isolated possible IRD deposition. ELT37_11_PC from George V Land exhibits low MS values across their length, reflecting reduced concentrations of magnetically susceptible minerals. MS values are slightly elevated in the upper ~250 cm (reaching up to $\sim 200 \times 10^{-5}$ SI) before decreasing and stabilizing at lower values ($\sim 50-100 \times 10^{-5}$ SI) downcore. This shift may reflect a change in sediment provenance or depositional regime, possibly linked to episodic lithogenic input.

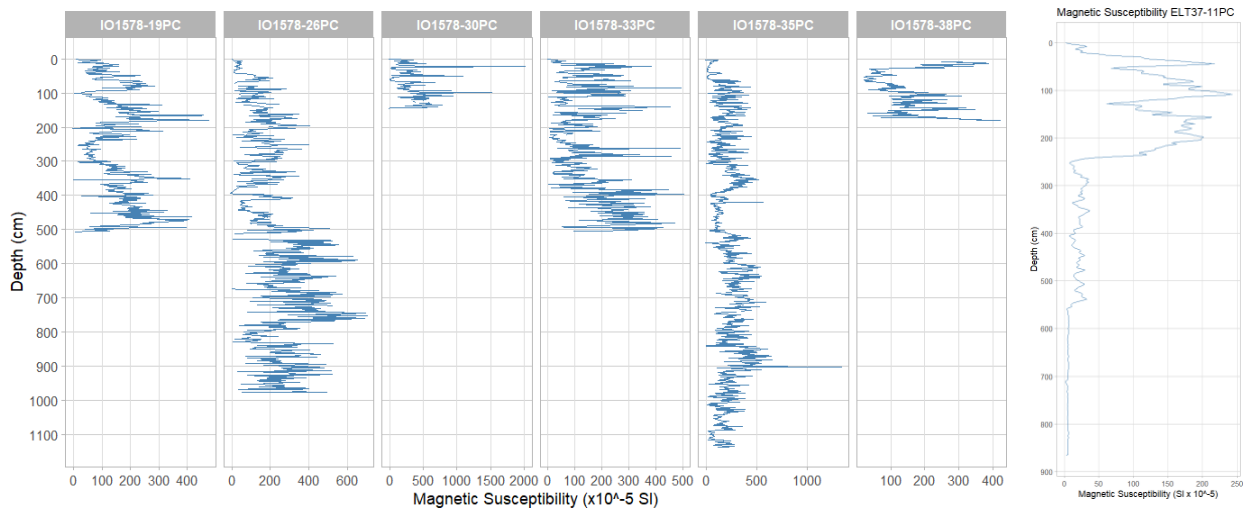


Figure 6. Downcore trend in magnetic susceptibility of the piston cores, excluding ELT37_15PC.

6. Discussion

6.1 IRD Index

To systematically evaluate the qualitative likelihood of IRD in samples, an IRD index is employed ranging from 0 to 4. This is then used to identify samples to separate from the full dataset that we believe represented the IRD population. The IRD index is based on the number of independent analytical indicators present in each sample, including (1) coarse grain size peaks (e.g., elevated D100 or multimodal LPSA distributions), (2) high magnetic susceptibility (MS) values, (3) enrichments in terrigenous elemental concentrations (Fe, Ti, K, Zr), and (4) clast presence in the original description of the core. Index values were assigned as follows:

0 – no IRD indicators present

1 – one indicator present

2 – two indicators

3 – three indicators

4 – all four indicators present

Although SEM was performed, it was not performed in all samples; therefore, it was not used in the index.

6.2 Regional Controls on Suspected IRD Delivery

The Weddell Sea continental slope cores (IO1578_19_PC, IO1578_26_PC, IO1578_35_PC) display frequent coarse-grained intervals characterized by elevated D100 values, multi-modal grain size distributions, and high MS and Fe-Ti concentrations (**Figures 3, 4, 5, 6**). These features align with lithogenic inputs previously attributed to iceberg rafting and glacial-proximal sedimentation along the Antarctic Margin (Passchier, 2011; Hillenbrand et al., 2009). In contrast, IO1578_30_PC and IO1578_33_PC exhibit fewer coarse peaks, lower MS values, and predominantly low suspected IRD index values (0–1), indicating more distal sedimentation or reduced IRD input to the shelf break and upper slope (**Figures 3, 4, 5**). Abyssal plain (IO1578_38_PC) and George V Land slope cores (ELT37_11_PC, ELT37_15_PC) similarly show fine-grained, unimodal distributions with consistently low MS and terrigenous element concentrations, characteristic of distal sedimentation with sporadic suspected IRD input (Passchier, 2011; Weber et al., 2014). The relative decrease in suspected IRD-bearing layers and lithogenic input in these distal settings highlights regional sediment supply differences, likely influenced by the configuration of glacial drainage systems and grounding line proximity (Prothro et al., 2018). SEM analysis of quartz grains from IO1578_26_PC (**Figure 6**) suggests the glacial origin of the coarse fraction, with the dominance of Type C glacial crushing textures—angular grains with striations, steps, and planar fractures—supporting subglacial erosion and iceberg delivery as primary transport mechanisms (Krissek, 1995; Passchier et al., 2021). The presence of Type D and E grains in selected samples indicates minor transport modification, consistent with short-distance reworking or sediment dispersal by ocean currents.

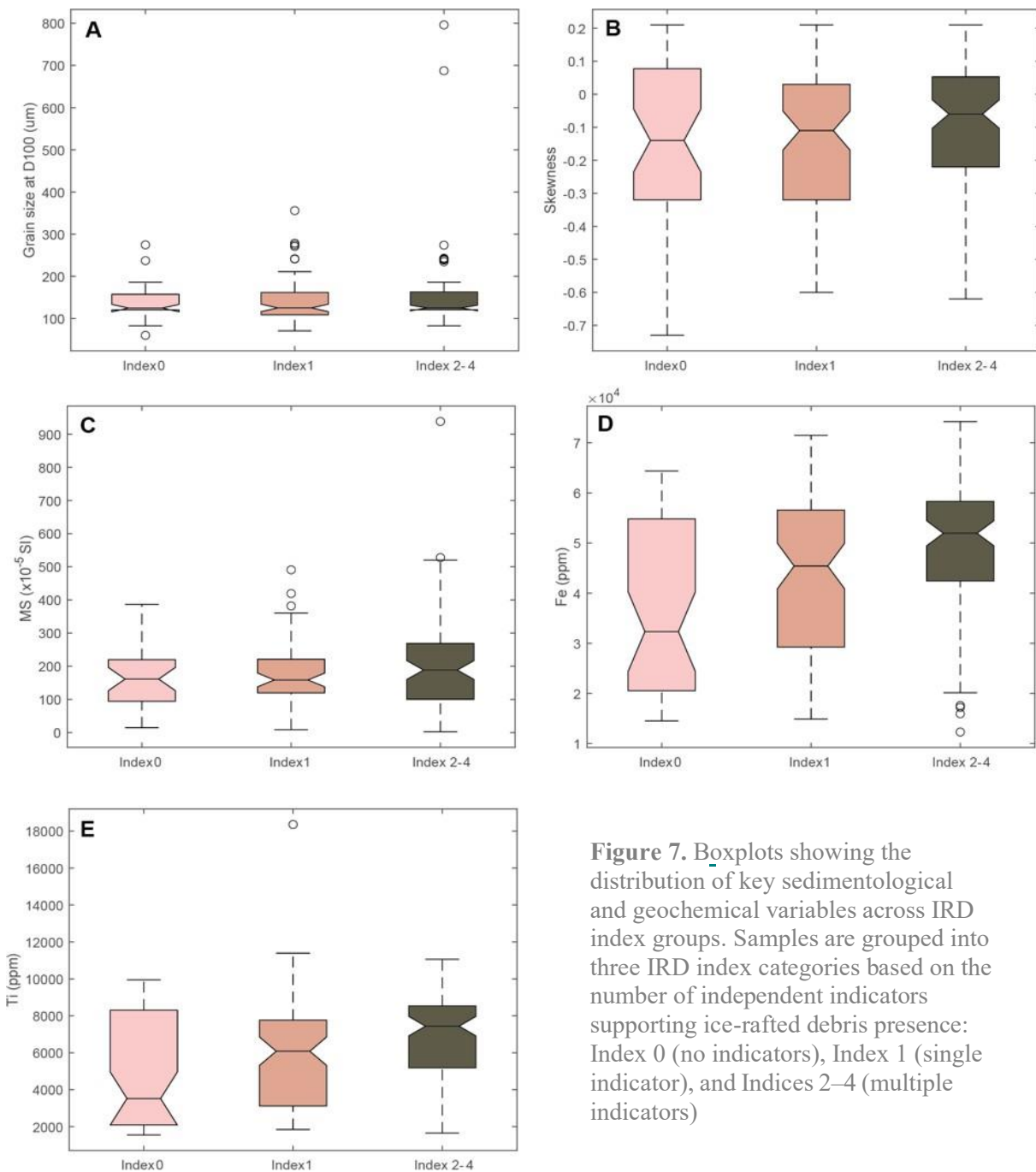


Figure 7. Boxplots showing the distribution of key sedimentological and geochemical variables across IRD index groups. Samples are grouped into three IRD index categories based on the number of independent indicators supporting ice-raftered debris presence: Index 0 (no indicators), Index 1 (single indicator), and Indices 2–4 (multiple indicators)

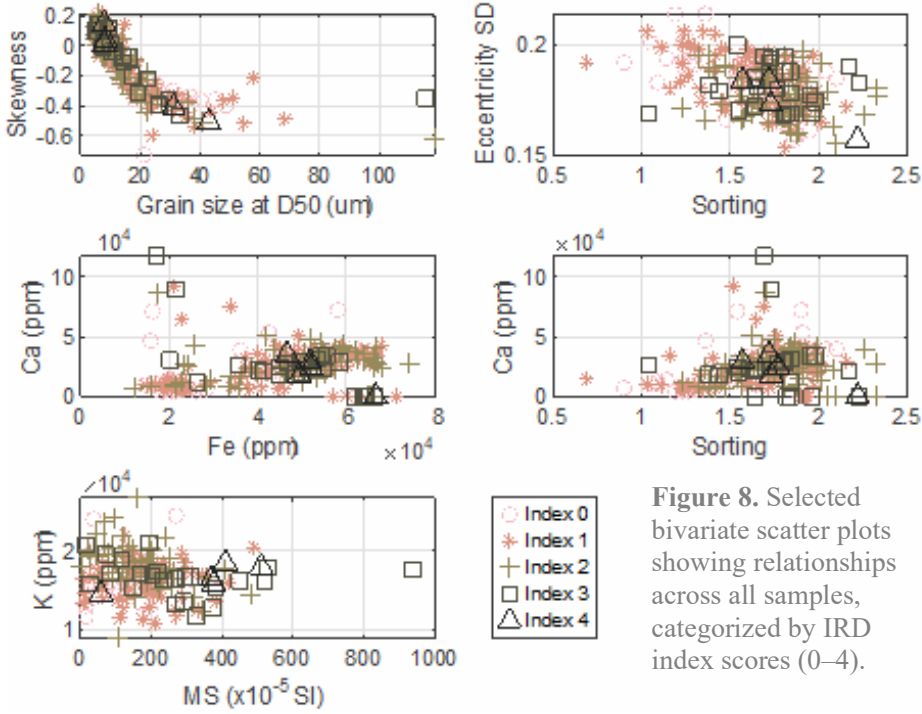


Figure 8. Selected bivariate scatter plots showing relationships across all samples, categorized by IRD index scores (0–4).

6.3 Relationships and Characteristics of Suspected IRD

Relationships among grain size, magnetic susceptibility (MS), and elemental concentrations were first evaluated using boxplots and bivariate scatterplots to examine variability within the dataset, especially of those variables that are often mentioned in published literature when identifying IRD in glaciomarine settings (Figures 7, 8). Distinct differences in the distribution of key variables, where samples containing coarser-grained sediment exhibit higher D100 values, elevated MS, and enriched Fe and Ti concentrations (Figure 7). In contrast, finer-grained samples are associated with lower MS and reduced elemental concentrations, reflecting a greater contribution of background hemipelagic sedimentation. Bivariate scatterplots reveal consistent relationships between grain size and other sedimentological variables across all cores (Figure 8). Larger grain sizes (D100) commonly co-occur with lower skewness, higher MS values, and increased Fe and Ti concentrations. These patterns are particularly well-developed in the Weddell Sea continental slope cores, where coarse-grained intervals are most abundant. To further quantify the strength of these relationships, Spearman correlation matrices were constructed for the full dataset (all samples) and for samples interpreted as IRD-bearing (Indices 2–4; Figure 9). Across all samples, D100, MS, and Fe-Ti concentrations exhibit strong positive correlations, consistent with the co-delivery of coarse sediment and lithogenic material. Additional moderate-to-strong positive correlations were observed between Ti and sorting, Ti and Fe, Ti and Zr, as well as Zr and

Ca, suggesting that terrigenous input is closely associated with both compositional and textural shifts in IRD-bearing intervals. Negative correlations were also noted between skewness and D50, as well as between circularity and the standard deviation of circularity, reinforcing inverse patterns in shape variability and symmetry. These relationships intensify when the analysis is restricted to IRD-bearing samples, highlighting the distinctive sedimentological signature associated with ice rafted debris deposition. Multivariate relationships are shown using principal component analysis (PCA) applied to samples with suspected IRD (**Figure 10**). Data incorporated into the PCA was standardized, so that differences in value magnitudes do not impact the outcomes. While the principal components 1 and 2 account for only 41.4% of the variance in the suspected IRD dataset, we see that principal component 1 is strongly influenced by skewness and moderately influenced by D50 and Zr, which cumulatively reflect a grain size control on variance. Taken together, PC1 represents grain size-driven variability in the dataset, while PC2 reflects compositional and transport-related influences, providing a two-axis framework for interpreting IRD variability in Antarctic margin sediments. Principal component 2 is dominated by MS, grain shape, sorting, and Ti, which together reflect composition and sediment transport/alteration controls on variance within the suspected IRD samples

Additionally, the biplot shows that Ti, Fe, sorting, and circularity are positively correlated, while MS is negatively correlated with Ca and eccentricity. A higher proportion of the suspected IRD plots in the negative principal component 1 and positive principal 2 space than in any other single quadrant; therefore, some key metrics to describe variance of IRD characteristics seem to be grain size distribution statistics (skewness, sorting), variation in grain circularity within individual samples, and terrigenous trace metals Fe and Ti.

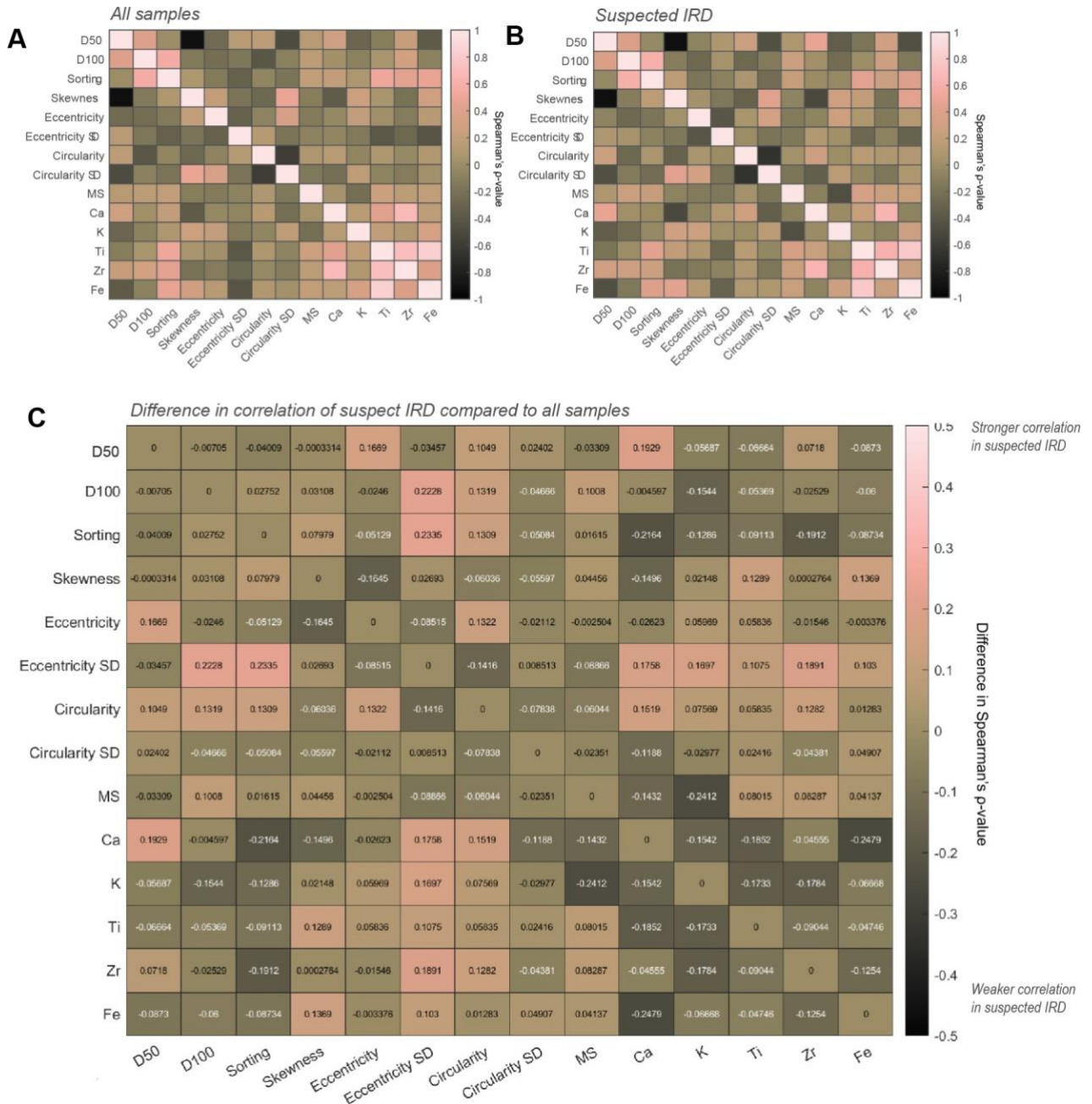


Figure 9. Correlation matrices of sedimentological and geochemical parameters. (A) Pairwise correlation matrix of all analyzed samples using grain size metrics, shape descriptors, geochemical elements, and magnetic susceptibility (MS). (B) Correlation matrix of samples interpreted as suspected IRD. (C) Matrix of differences between the suspected IRD subset and the full dataset. Warmer colors indicate stronger correlations, while cooler tones reflect negative.

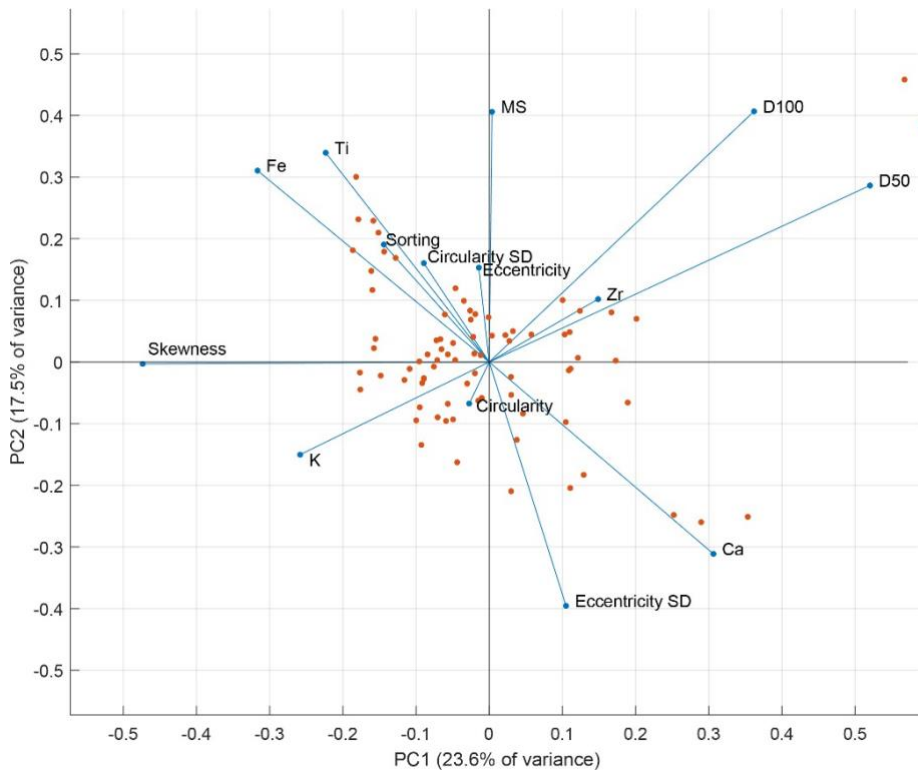


Figure 10. Biplot of suspected IRD samples (indices 2–4), show the first two principal components (PC; PC1: 23.6% of variance, PC2: 17.5%) showing the direction and contribution of each variable relative to the scores of samples (orange dots).

6.4 Recommendations for identifying IRD offshore of Antarctica

Identifying ice-rafted debris (IRD) in glaciomarine sediments—particularly in fine-grained Antarctic margin settings—requires a robust and flexible analytical strategy. Based on the results of this study, the following recommendations outline key methodological considerations for improving the detection, classification, and interpretation of IRD. These suggestions aim to guide future sedimentological and paleoenvironmental studies focused on reconstructing Antarctic Ice Sheet variability.

1. Adopt a Multiproxy Framework

Relying on a single indicator, such as grain size or visual clast abundance, may overlook fine-grained IRD. Integrating grain size (D100, sorting, skewness), magnetic susceptibility (MS), elemental geochemistry (Fe, Ti, Zr, K), and SEM microtextures offers a more comprehensive and reliable means of IRD identification.

Among these, maximum grain size (D100), magnetic susceptibility, and Fe–Ti concentrations emerged as the most robust and consistent indicators of IRD-bearing

intervals in this study. These variables exhibited strong covariation in statistical analyses and were most effective at distinguishing IRD from background sedimentation.

2. Implement an IRD Index Systematically

The IRD index (0–4), developed in this study, allows for standardized classification of IRD-bearing intervals based on the presence of multiple independent proxies. This tool is particularly valuable when coarse clasts are rare or absent. Future studies should consider adapting and applying this index to other Antarctic margin cores to facilitate inter-site comparisons.

3. Emphasize Core Context and Depositional Setting

Sedimentological context is critical. Cores from the continental slope exhibited higher IRD index values compared to abyssal plain or more distal settings. Thus, interpreting IRD should account for spatial variations in sediment supply, grounding line proximity, and depositional energy.

4. Expand Use of High-Resolution Imaging

SEM imaging proved vital in identifying glacial crushing textures in fine fractions, especially where coarse proxies were absent. Continued use of SEM and possibly CT scans for clast identification can improve resolution and confidence in IRD attribution.

5. Incorporate Additional Chronological and Biological Proxies

Future research should integrate Pb²¹⁰ and radiocarbon dating, along with microfossil (e.g., diatom) assemblages, to link IRD layers with precise environmental changes and validate depositional timing.

6. Promote Data Comparability and Standardization

Standardizing analytical protocols (e.g., sieve thresholds, MS calibration, XRF settings) and publishing datasets with IRD index scores will enhance reproducibility and enable broader-scale syntheses across Antarctic regions.

7. Conclusions and Future Work

This study demonstrates that a multiproxy approach substantially improves the identification of fine-grained ice-rafter debris (IRD) in Antarctic margin sediments compared to reliance on single proxies. By integrating grain size statistics, magnetic susceptibility (MS), elemental geochemistry, grain shape analysis, and scanning electron microscopy (SEM), the framework developed here enables more robust detection of IRD-bearing intervals, including those lacking coarse clasts or visual indicators.

Laser particle size analysis (LPSA) provided multimodal distributions and poor sorting consistent with stochastic IRD delivery, but alone could not differentiate IRD from other glacial sediment types. MS and elemental geochemistry (Fe, Ti, K, Zr) strengthened IRD identification by capturing lithogenic input patterns associated with iceberg rafting and glacial erosion. SEM analysis further

confirmed subglacial transport mechanisms through microtextural evidence, particularly in fine-grained layers where traditional proxies were ambiguous.

A semi-quantitative IRD index (ranging from 0–4 based on the presence of independent indicators) was developed to classify and compare IRD-bearing samples across depositional environments. This index, supported by correlation matrices and principal component analysis, revealed distinct sedimentological signatures associated with suspected IRD and highlighted regional variability in delivery processes. The highest abundance and variability of IRD were observed in the Weddell Sea continental slope cores, while abyssal and George V Land slope cores reflected finer, more uniform sedimentation and reduced IRD input.

Future studies should refine this multiproxy framework by incorporating additional proxies such as CT-scan clast counts and expanding chronological control through radiocarbon and ^{210}Pb dating, alongside diatom assemblage analysis. Such integration will enhance temporal resolution and allow for a more comprehensive reconstruction of Antarctic Ice Sheet variability in response to environmental forcing across centennial to millennial timescales.

8. References

- Adusumilli, S., Fricker, H. A., Medley, B., Padman, L., & Siegfried, M. R. (2020). Interannual variations in meltwater input to the Southern Ocean from Antarctic ice shelves. *Nature Geoscience*, 13(9), 616-620.
- Alley, R. B., & MacAyeal, D. R. (1994). Ice rafted debris associated with binge/purge oscillations of the Laurentide Ice Sheet. *Paleoceanography*, 9(4), 503-511.
- Anderson, J. B., & Andrews, J. T. (1999). Radiocarbon constraints on ice sheet advance and retreat in the Weddell Sea, Antarctica. *Geology*, 27(2), 179–182.
- Anderson, J. B., Kurtz, D. D., Domack, E. W., & Balshaw, K. M. (1980). Glacial and glacial marine sediments of the Antarctic continental shelf. *The Journal of Geology*, 88(4), 399-414.
- Anderson, J. B. (1972). Nearshore glacial-marine deposition from modern sediments of the Weddell Sea. *Nature Physical Science*, 240(104), 189-192.
- Andrews, J. (2000). Icebergs and iceberg rafted detritus (IRD) in the North Atlantic: Facts and assumptions. *Oceanography*, 13(3), 100–108. <https://doi.org/10.5670/oceanog.2000.19>
- Andrews, J.T., Voelker, A.H., 2018. “Heinrich events” (& sediments): A history of terminology and recommendations for future usage. *Quat. Sci. Rev.* 187, 31–40. <https://doi.org/10.1016/j.quascirev.2018.03.017>.
- B. K. Lucchitta, H. M. Ferguson, Antarctica: Measuring Glacier Velocity from Satellite Images. *Science* 234, 1105-1108 (1986). DOI:10.1126/science.234.4780.1105
- Campagne, P., Crosta, X., Schmidt, S., Noëlle Houssais, M., Ther, O., and Massé, G.: Sedimentary response to sea ice and atmospheric variability over the instrumental period off Adélie Land, East Antarctica, *Biogeosciences*, 13, 4205–4218,

- <https://doi.org/10.5194/bg-13-4205-2016>, 2016.
- Cazenave, A., Meyssignac, B., Ablain, M., Balmaseda, M., Bamber, J., Barletta, V., ... & Wouters, B. (2018). Global sea-level budget 1993-present. *Earth System Science Data*, 10(3), 1551-1590.
- Columbia Climate School Lamont-Doherty, E. O. (n.d.). Retrieved from Types of cores: <https://corerepository.ldeo.columbia.edu/content/types-samples>
- Depoorter, M. A., Bamber, J. L., Griggs, J. A., Lenaerts, J. T. M., Ligtenberg, S. R. M., van den Broeke, M. R., & Moholdt, G. (2013). Calving fluxes and basal melt rates of Antarctic ice shelves. *Nature*, 502, 89–92. <https://doi.org/10.1038/nature12567>
- Diekmann, B., Kuhn, G., Kopsch, C., & Abelmann, A. (2003). Terrigenous sediment supply in the polar to temperate South Atlantic: Land–ocean links of environmental changes during the late Quaternary. In *Marine Geology*, 201(1-3), 1–18. [https://doi.org/10.1016/S0025-3227\(03\)00153-8](https://doi.org/10.1016/S0025-3227(03)00153-8)
- Dunnington, D. W., Roberts, S., Norton, S. A., Spooner, I. S., Kurek, J., Kirk, J. L., ... & Gagnon, G. A. (2020). Over two centuries, the distribution and transport of lead was recorded by lake sediments from northeastern North America. *Science of the Total Environment*, 737, 140212. <https://doi.org/10.1016/j.scitotenv.2020.140212>
- Elverhøi, A. (1981). Evidence for a late Wisconsin glaciation of the Weddell Sea. *Nature*, 293(5834), 641–642.
- Etourneau, J., Collins, L. G., Willmott, V., Kim, J.-H., Barbara, L., Leventer, A., Schouten, S., Sinninghe Damsté, J. S., Bianchini, A., Klein, V., Crosta, X., and Massé, G.: Holocene climate variations in the western Antarctic Peninsula: evidence for sea ice extent predominantly controlled by changes in insolation and ENSO variability, *Clim. Past*, 9, 1431–1446, <https://doi.org/10.5194/cp-9-1431-2013>, 2013.
- Evans, M.E., Heller, F., Bloemendal, J., & Thouveny, N. (1997). Natural Magnetic Archives of Past Global Change. *Surveys in Geophysics*, 18(2), 183–196. <https://doi.org/10.1023/A:1006583809200>
- Favier, L., Durand, G., Cornford, S. L., Gudmundsson, G. H., Gagliardini, O., Gillet-Chaulet, F., & Le Brocq, A. M. (2014). Retreat of Pine Island Glacier controlled by marine icesheet instability. *Nature Climate Change*, 4(2), 117-121.
- Folk, R. L., and Ward, W. C. (1957). Brazos River Bar [Texas]; a Study in the Significance of Grain Size Parameters. *J. Sediment. Res.* 27 (1), 3–26. doi:10.1306/74d70646-2b21-11d7-8648000102c1865d
- Fox-Kemper, B., H. T. Hewitt, C. Xiao, G. Aðalgeirsdóttir, S. S. Drijfhout, ... & Y. Yu, 2021, Ocean, Cryosphere and Sea Level Change. In: Climate Change 2021: The Physical Science Basis. Contribution of Working Group I to the Sixth Assessment Report of the Intergovernmental Panel on Climate Change [Masson-Delmotte, V., P. Zhai, A. Pirani, S. L. Connors, C. Péan, S. Berger, N. Caud, Y. Chen, L. Goldfarb, M. I. Gomis, M. Huang, K. Leitzell, E. Lonnoy, J.B.R. Matthews, T. K. Maycock, T. Waterfield, O.

- Yelekçi, R. Yu and B. Zhou (eds.)]. Cambridge University Press.
- Hahn, A., Gerdts, G., Völker, C. and Niebühr, V., 2019. I am using FTIRS as pre-screening method for detection of microplastic in bulk sediment samples. *Science of the total environment*, 689, pp.341-346. <https://doi.org/10.1016/j.scitotenv.2019.06.227>
- Hawkins, J. R., Skidmore, M. L., Wadham, J. L., Priscu, J. C., Morton, P. L., Hatton, J. E., ... & Spencer, R. G. (2020). Enhanced trace element mobilization by Earth's ice sheets. *Proceedings of the National Academy of Sciences*, 117(50), 31648-31659.
- Hemming, S. R. (2004). Heinrich events: Massive late Pleistocene detritus layers of the North Atlantic and their global climate imprint, *Rev. Geophys.*, 42, RG1005, doi:10.1029/2003RG000128.
- Hill, E.A., Gudmundsson, G.H. & Chandler, D.M. Ocean warming as a trigger for irreversible retreat of the Antarctic ice sheet. *Nat. Clim. Chang.* 14, 1165–1171 (2024). <https://doi.org/10.1038/s41558-024-02134-8>
- Hillenbrand, C.-D., Kuhn, G., & Frederichs, T. (2009). Record of a Mid-Pleistocene depositional anomaly in West Antarctic continental margin sediments: An indicator for ice-sheet collapse? *Quaternary Science Reviews*, 28((13–14)), 1147–1159. <https://doi.org/10.1016/j.quascirev.2008.12.010>
- Hillenbrand, C.D., Melles, M., Kuhn, G., Larter, R.D., 2012. Marine geological constraints for the grounding-line position of the Antarctic Ice Sheet on the southern Weddell Sea shelf at the Last Glacial Maximum. *Quaternary Science Reviews* 32, 25e47.
- Hillenbrand, C. D., Bentley, M. J., Stolldorf, T. D., Hein, A. S., Kuhn, G., Graham, A. G., ... & Sugden, D. E. (2014). Reconstruction of changes in the Weddell Sea sector of the Antarctic Ice Sheet since the Last Glacial Maximum. *Quaternary Science Reviews*, 100, 111-136. <https://doi.org/10.1016/j.quascirev.2013.07.020>
- Jansen, E., T. Fronval, F. Rack, and J. E. T. Channell (2000), Pliocene-Pleistocene ice rafting history and cyclicity in the Nordic Seas during the last 3.5 Myr, *Paleoceanography*, 15(6), 709–721, doi:10.1029/1999PA000435.
- Jena, B., Bajish, C.C., Turner, J. et al. Record low sea ice extent in the Weddell Sea, Antarctica in April/May 2019 driven by intense and explosive polar cyclones. *npj Clim Atmos Sci* 5, 19 (2022). <https://doi.org/10.1038/s41612-022-00243-9>
- Jenkins, A., Shoosmith, D., Dutrieux, P., Jacobs, S., Kim, T. W., Lee, S. H., ... & Stammerjohn, S. (2018). West Antarctic Ice Sheet retreat in the Amundsen Sea driven by decadal oceanic variability. *Nature Geoscience*, 11(10), 733-738.
- Lepp, A. P., Miller, L. E., Anderson, J. B., O'Regan, M., Winsborrow, M. C. M., Smith, J. A., Hillenbrand, C.-D., Wellner, J. S., Prothro, L. O., and Podolskiy, E. A.: Insights into glacial processes from micromorphology of silt-sized sediment, *The Cryosphere*, 18, 2297–2319, <https://doi.org/10.5194/tc-18-2297-2024>, 2024.
- Lepp AP, Simkins LM, Anderson JB, Clark RW, Wellner JS, Hillenbrand C-D, Smith JA, Lehrmann AA, Totten R, Larter RD, Hogan KA, Nitsche FO, Graham AGC and

- Wacker L (2022) Sedimentary Signatures of Persistent Subglacial Meltwater Drainage from Thwaites Glacier, Antarctica. *Front. Earth Sci.* 10:863200. doi: 10.3389/feart.2022.863200
- Lucchitta BK, Ferguson HM. Antarctica: measuring glacier velocity from satellite images. *Science*. 1986 Nov 28;234(4780):1105-8. doi: 10.1126/science.234.4780.1105. PMID: 17778951.
- Lyle, M., Heusser, L., Ravelo, C., Yamamoto, M., Barron, J., Diffenbaugh, N.S., Herbert, T. and Andreasen, D., 2012. Out of the tropics: the Pacific, Great Basin Lakes, and Late Pleistocene water cycle in the western United States. *science*, 337(6102), pp.1629-1633. DOI:10.1126/science.1218390
- McKay, R., Albot, O., Dunbar, G. B., Lee, J. I., Lee, M. K., Yoo, K.-C., et al. (2022). A comparison of methods for identifying and quantifying ice rafted debris on the Antarctic margin. *Paleoceanography and Paleoclimatology*, 37, e2021PA004404. <https://doi.org/10.1029/2021PA00440431>
- Medley, B., Thomas, E.R. Increased snowfall over the Antarctic Ice Sheet mitigated twentieth-century sea-level rise. *Nature Clim Change* 9, 34–39 (2019). <https://doi.org/10.1038/s41558-018-0356-x>
- National Academies of Sciences, Engineering, and Medicine 2021. Mid-Term Assessment of Progress on the 2015 Strategic Vision for Antarctic and Southern Ocean Research. Washington, DC: The National Academies Press.
- National Academies of Sciences, Engineering, and Medicine 2015. A Strategic Vision for NSF Investments in Antarctic and Southern Ocean Research. Washington, DC: The National Academies Press.
- Ó Cofaigh, C., Dowdeswell, J. A., & Pudsey, C. J. (2001). Late Quaternary ice rafting events in the northern Weddell Sea, Antarctica: Implications for Antarctic glacial history from sediment provenance studies. *Marine Geology*, 172(1-2), 59–84. [https://doi.org/10.1016/S0025-3227\(00\)00167-5](https://doi.org/10.1016/S0025-3227(00)00167-5)
- Passchier, S. (2011). Linkages between East Antarctic ice sheet extent and Southern Ocean temperatures based on a Pliocene high-resolution record of ice-rafted debris off Prydz Bay, East Antarctica. *Paleoceanography*, 26, 13 PP. <https://doi.org/10.1029/2010PA002061>
- Patterson, M. O., McKay, R., Naish, T., Escutia, C., Jimenez-Espejo, F. J., Raymo, M. E., et al. (2014). Orbital forcing of the east Antarctic ice sheet during the Pliocene and early Pleistocene. *Nature Geoscience*, 7(11), 841–847. <https://doi.org/10.1038/ngeo2273>
- Pirrung, M., Fütterer, D., Grobe, H. et al. Magnetic susceptibility and ice-rafted debris in surface sediments of the Nordic Seas: implications for Isotope Stage 3 oscillations. *GeoMar Lett* 22, 1–11 (2002). <https://doi.org/10.1007/s00367-002-0090-1>
- Pruysers, P. A., de Lange, G. J., & Middelburg, J. J. (1991). Geochemistry of eastern Mediterranean sediments: Primary sediment composition and diagenetic alterations.

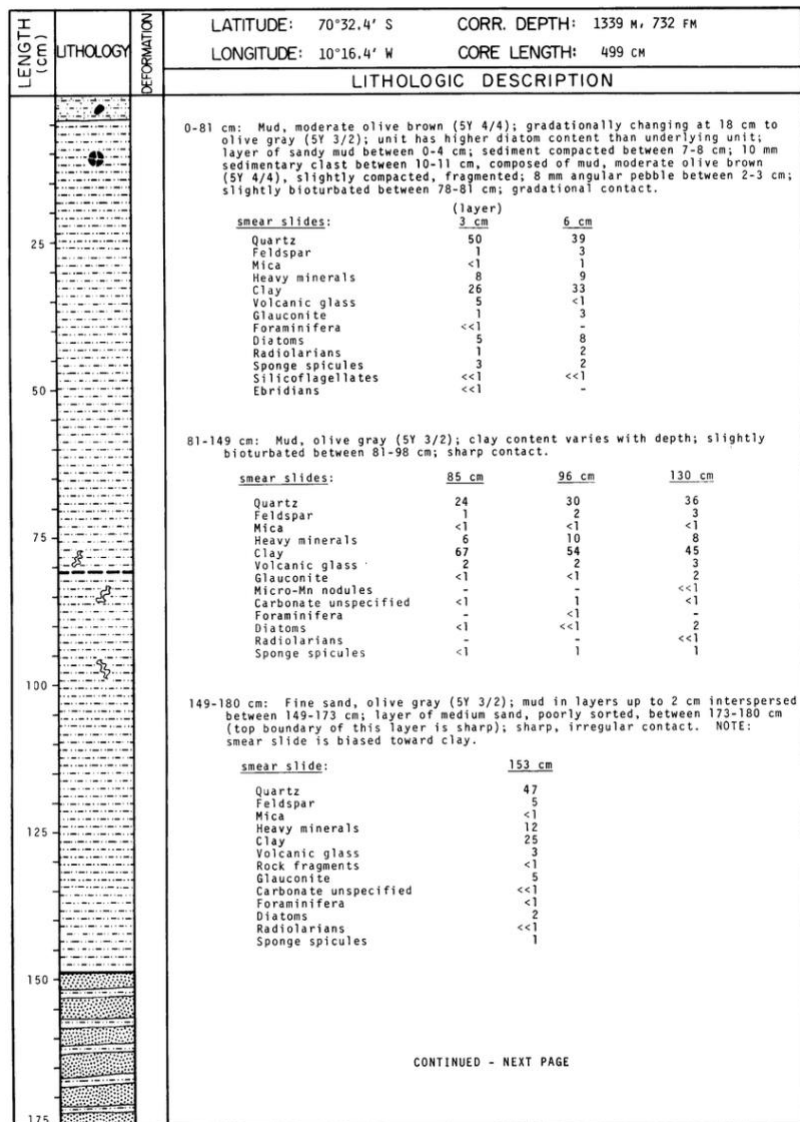
- Marine Geology, 100(1-4), 137-154.
- Pudsey, C.J. and Howe, J.A., 1998. Quaternary history of the Antarctic Circumpolar Current: evidence from the Scotia Sea. *Marine Geology*, 148(1-2), pp.83-112.
[https://doi.org/10.1016/S0025-3227\(98\)00014-0](https://doi.org/10.1016/S0025-3227(98)00014-0)
- Rignot, E., Mouginot, J., Scheuchl, B., Van Den Broeke, M., Van Wessem, M. J., & Morlighem, M. (2019). Four decades of Antarctic Ice Sheet mass balance from 1979–2017. *Proceedings of the National Academy of Sciences*, 116(4), 1095-1103.
- Ritz, C., Edwards, T., Durand, G. et al. Potential sea-level rise from Antarctic ice-sheet instability constrained by observations. *Nature* 528, 115–118 (2015).
<https://doi.org/10.1038/nature16147>
- Riva, R. E. M., J. L. Bamber, D. A. Lavallée, and B. Wouters (2010), Sea-level fingerprint of continental water and ice mass change from GRACE, *Geophys. Res. Lett.*, 37, L19605, doi:10.1029/2010GL044770. 32
- Rothwell, R. G. (2015). Twenty years of XRF core scanning marine sediments: what do geochemical proxies tell us?. In *Micro-XRF studies of sediment cores* (pp. 25-102). Springer, Dordrecht.
- Schoof, C. (2012). Marine ice sheet stability. *Journal of Fluid Mechanics*, 698, 62-72.
- Sharon L. Kanfoush et al., Millennial-Scale Instability of the Antarctic Ice Sheet During the Last Glaciation. *Science* 288, 1815-1819(2000). DOI:10.1126/science.288.5472.1815
- Shepherd, A., Ivins, E. R., Geruo, A., Barletta, V. R., Bentley, M. J., Bettadpur, S., ... & Zwally, H. J. (2012). A reconciled estimate of ice-sheet mass balance. *Science*, 338(6111), 1183-1189.
- Stolldorf, T., Schenke, H. W., & Anderson, J. B. (2012). LGM ice sheet extent in the Weddell Sea: evidence for diachronous behavior of Antarctic Ice Sheets. *Quaternary Science Reviews*, 48, 20-31.
- Weber, M. E., Clark, P. U., Kuhn, G., Timmermann, A., Sprenk, D., Gladstone, R., et al. (2014). Millennial-scale variability in Antarctic ice-sheet discharge during the last deglaciation. *Nature*, 510(7503), 134–138. <https://doi.org/10.1038/nature13397>
- Williams, T., van de Flierdt, T., Hemming, S. R., Chung, E., Roy, M., & Goldstein, S. L. (2010). Evidence for iceberg armadas from East Antarctica in the Southern Ocean during the late Miocene and early Pliocene. *Earth and Planetary Science Letters*, 290(3–4), 351–361. <https://doi.org/10.1016/j.epsl.2009.12.031>
- Ziegler, M., Jilbert, T., de Lange, G. J., Lourens, L. J., & Reichart, G. J. (2008). Bromine counts from XRF scanning as an estimate of the marine organic carbon content of sediment cores. *Geochemistry, Geophysics, Geosystems*, 9(5).

APPENDIX 1

Weddell Sea Cores

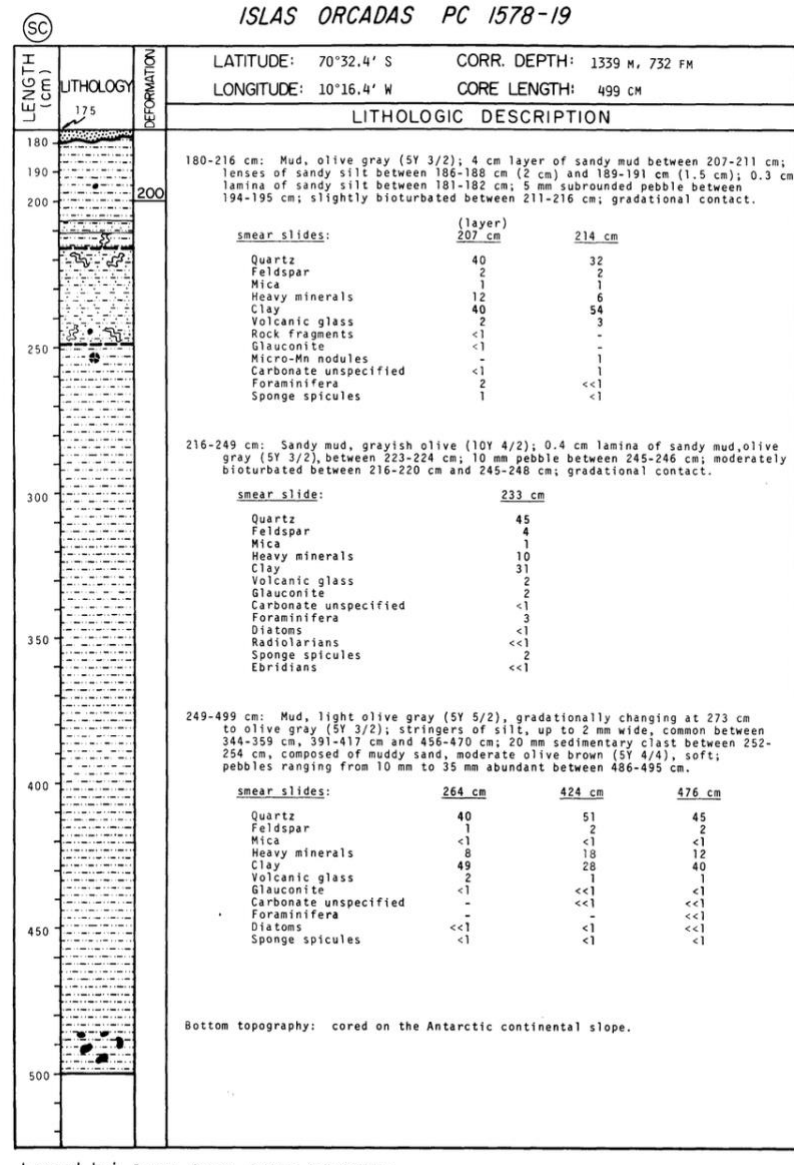
CRUISE: IO1578 CORE_ID: 19 TYPE: PC

ISLAS ORCADAS PC 1578-19



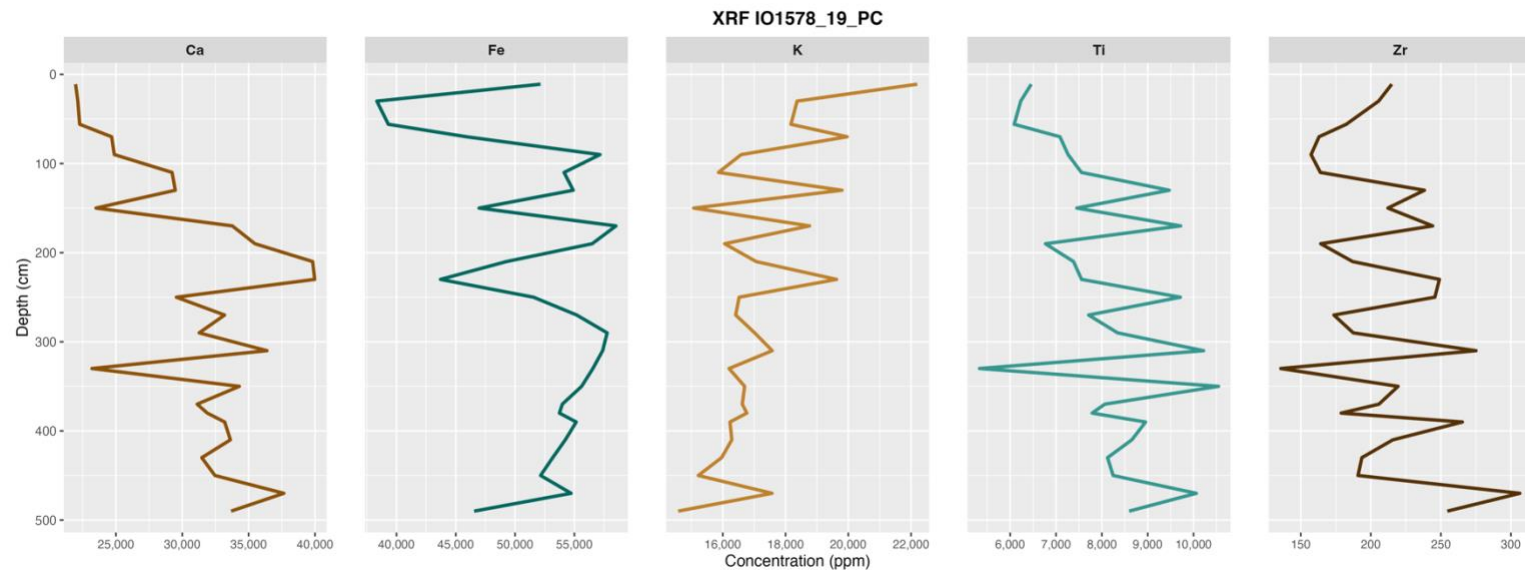
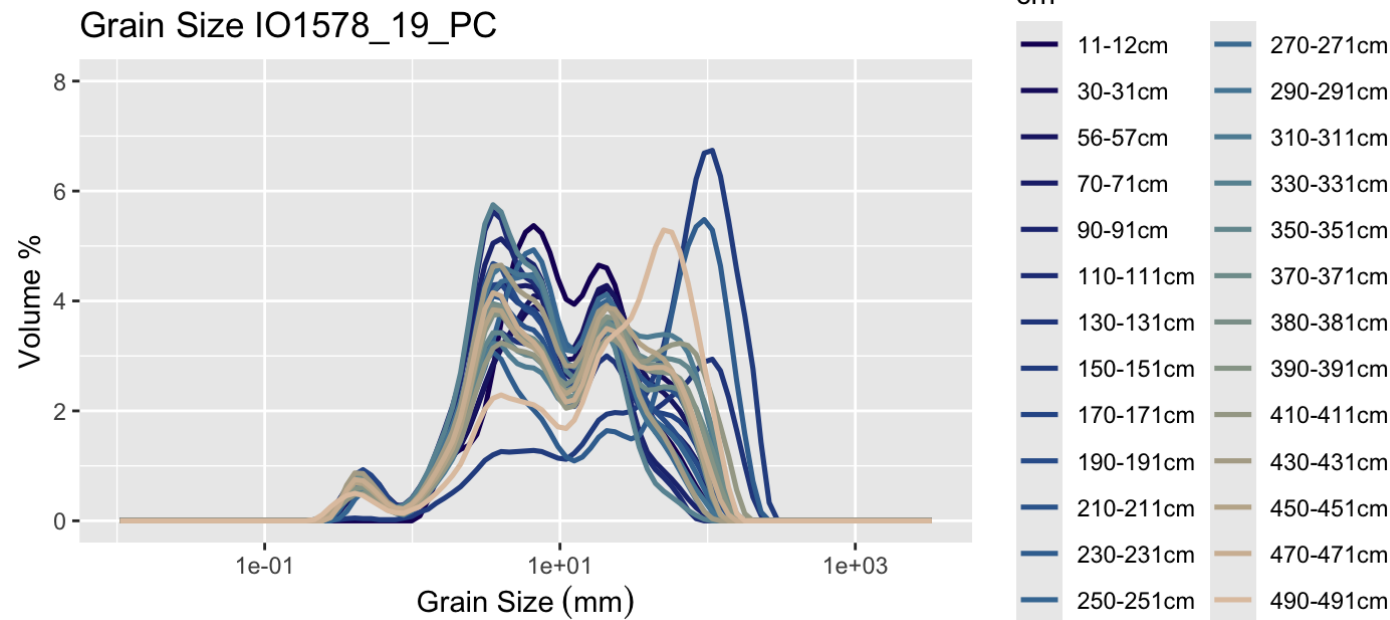
Logged by: Eggers, Graves, Bergen, Kaharoeddin

ISLAS ORCADAS PC 1578-19



Logged by: Eggers, Graves, Bergen, Kaharoeddin

CRUISE: IO1578 CORE_ID: 19 TYPE: PC



ISLAS ORCADAS PC 1578-26

LENGTH (cm)	LITHOLOGY	DEFORMATION	LITHOLOGIC DESCRIPTION		
			LATITUDE: 71°54.1' S	CORR. DEPTH: 2242 M, 1226 FM	
			LONGITUDE: 17°15.6' W	CORE LENGTH: 1135 CM	
0-47			0-47 cm: Mud, light olive gray (5Y 5/2); highly disturbed between 15-32 cm; slightly disturbed between 0-15 cm and 32-45 cm; disturbances due to freezing of the core; gradational contact.		
71			smear slide: 6 cm		
			Quartz 38		
			Feldspar 2		
			Mica 1		
			Heavy minerals 8		
			Clay 41		
			Volcanic glass 2		
			Glauconite 3		
			Diatoms 4		
			Radiolarians <1		
			Sponge spicules 1		
150			47-358 cm: Silt, light olive gray (5Y 5/2), gradationally changing to olive gray (5Y 3/2) at 69 cm; size of silt varies from fine to coarse, poorly sorted, predominantly composed of quartz and heavy minerals; higher foraminiferal content between 309-337 cm; lower clay content between 320-358 cm; laminae of coarse silt common between 207-284 cm, sparsely interspersed between 73-207 cm; 29 mm subrounded pebble between 68-71 cm; 10 mm angular pebble between 269-271 cm; 15 mm subangular pebble between 331-333 cm; moderately disturbed between 309-335 cm; slightly disturbed between 304-307 cm; disturbances due to freezing of the core; gradational contact.		
225			smear slides: 64 cm 199 cm 303 cm		
			Quartz 60	55	50
			Feldspar 3	2	2
			Mica <1	<1	1
			Heavy minerals 15	16	15
			Clay 17	22	21
			Volcanic glass 2	3	4
			Glauconite 2	2	2
			Carbonate unspecified <1	-	1
			Foraminifera <<1	<<1	<3
			Diatoms <1	<<1	<<1
			Radiolarians <1	<<1	-
			Sponge spicules <1	<1	1
			Silicoflagellates <<1	-	-
300			358-474 cm: Mud, light olive gray (5Y 5/2); highly bioturbated between 358-369 cm; slightly bioturbated between 369-405 cm; gradational contact.		
375			smear slides: 371 cm 414 cm		
			Quartz 39	40	
			Feldspar 3	2	
			Mica 1	1	
			Heavy minerals 10	15	
			Clay 42	37	
			Volcanic glass 3	2	
			Glauconite 2	2	
			Diatoms <1	<1	
			Radiolarians -	<<1	
			Sponge spicules <1	1	
450			474-524 cm: Mud, light olive gray (5Y 5/2), gradationally changing to olive gray (5Y 3/2) at 474 cm; stringers of silt, composed primarily of quartz particles, between 502-503 cm and 508-509 cm; 10 mm subangular pebble between 492-493 cm; slightly disturbed between 490-495 cm due to freezing of the core; sharp contact.		
510			smear slide: 492 cm		
			Quartz 55	Volcanic glass 1	
			Feldspar 2	Glauconite 2	
			Mica 2	Diatoms <1	
			Heavy minerals 10	Sponge spicules <1	
			Clay 28		
525			CONTINUED - NEXT PAGE		

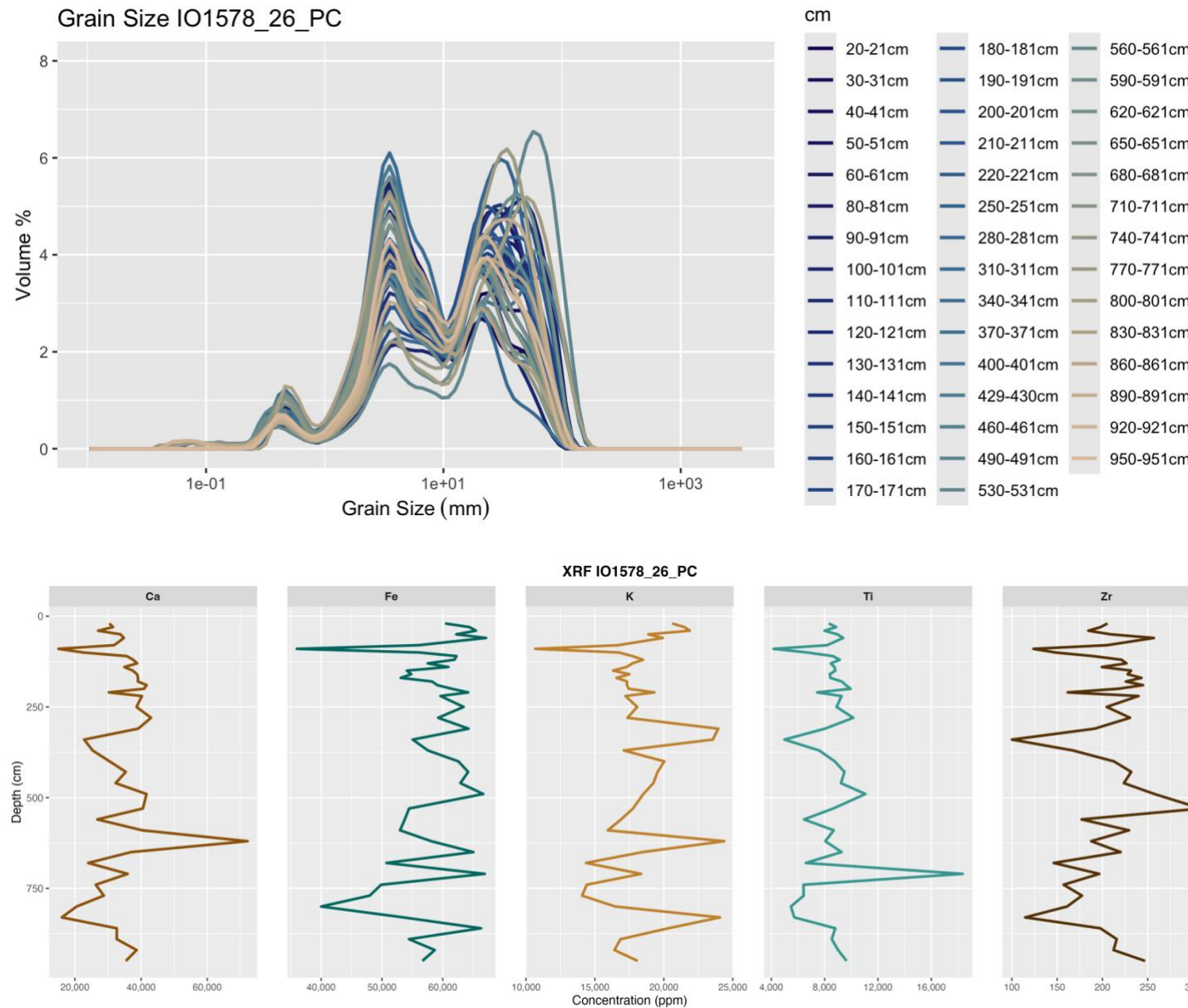
ISLAS ORCADAS PC 1578-26

LENGTH (cm)	LITHOLOGY	DEFORMATION	LITHOLOGIC DESCRIPTION		
530			524-566 cm: Sandy mud, olive gray (5Y 3/2); sharp contact.		
550			smear slide: 528 cm		
			Quartz 57	Glauconite 2	
			Feldspar 2	Carbonate unspecified <1	
			Mica 1	Foraminifera 2	
			Heavy minerals 14	Diatoms <<1	
			Clay 20	Sponge spicules <1	
			Volcanic glass 2		
650			566-799 cm: Mud, olive gray (5Y 3/2), gradationally changing to olive gray (5Y 4/2) between 776-799 cm; highly laminated with laminae of coarse, silt-size quartz particles between 573-595 cm and between 745-775 cm; moderately laminated with laminae of medium, silt-size quartz particles between 686-745 cm; slightly laminated with laminae of medium, silt-size quartz particles between 624-686 cm; 1 cm lamina of clay, light olive gray (5Y 5/2), between 798-799 cm; subangular pebbles between 576-578 cm (14 mm), 652-653 cm (7 mm), 731-733 cm (19 mm) and 774-776 cm (12 mm); slightly bioturbated between 621-649 cm; sharp, wavy contact.		
750			smear slides: 570 cm 771 cm 570 cm 771 cm		
			Quartz 45	Glauconite 1	
			Feldspar 2	Carbonate unspecified <<1	
			Mica 1	Foraminifera <<1	
			Heavy minerals 11	Diatoms <<1	
			Clay 37	Sponge spicules -	
			Volcanic glass 3		1
850			799-821 cm: Diatomaceous mud, olive gray (5Y 4/1); zone of higher silt content between 799-803 cm; gradational contact.		
			smear slide: 812 cm		
			Quartz 40	Glauconite 2	
			Feldspar 1	Diatoms 15	
			Mica <1	Radiolarians <1	
			Heavy minerals 11	Sponge spicules 1	
			Clay 26	Silicoflagellates <<1	
			Volcanic glass 4		
950			821-938 cm: Mud, olive gray (5Y 3/2); moderately laminated with laminae of medium, silt-size quartz particles between 885-890 cm; slightly laminated between 918-919 cm; stringers of silt between 924-930 cm; subangular pebbles between 914-916 cm (10 mm) and 922-923 cm (5 mm); 18 mm subrounded pebble between 931-933 cm; gradational contact.		
			smear slide: 858 cm		
			Quartz 45	Volcanic glass 3	
			Feldspar 2	Glauconite 1	
			Mica <1	Diatoms <1	
			Heavy minerals 15	Radiolarians <<1	
			Clay 33	Sponge spicules 1	
1050		FLOW-IN	938-1135 cm: Mud, grayish olive (10Y 4/2); higher silt content than in overlying unit; 10 mm subrounded pebble between 945-946 cm; 5 mm subangular pebble between 953-954 cm; gradationally changing to flow-in at 955 cm.		
			smear slide: 954 cm		
			Quartz 48	Volcanic glass 1	
			Feldspar 2	Glauconite 1	
			Mica <1	Diatoms <<1	
			Heavy minerals 11	Sponge spicules 1	
			Clay 36		
1150			Bottom topography: gently sloping; on the Antarctic continental slope.		

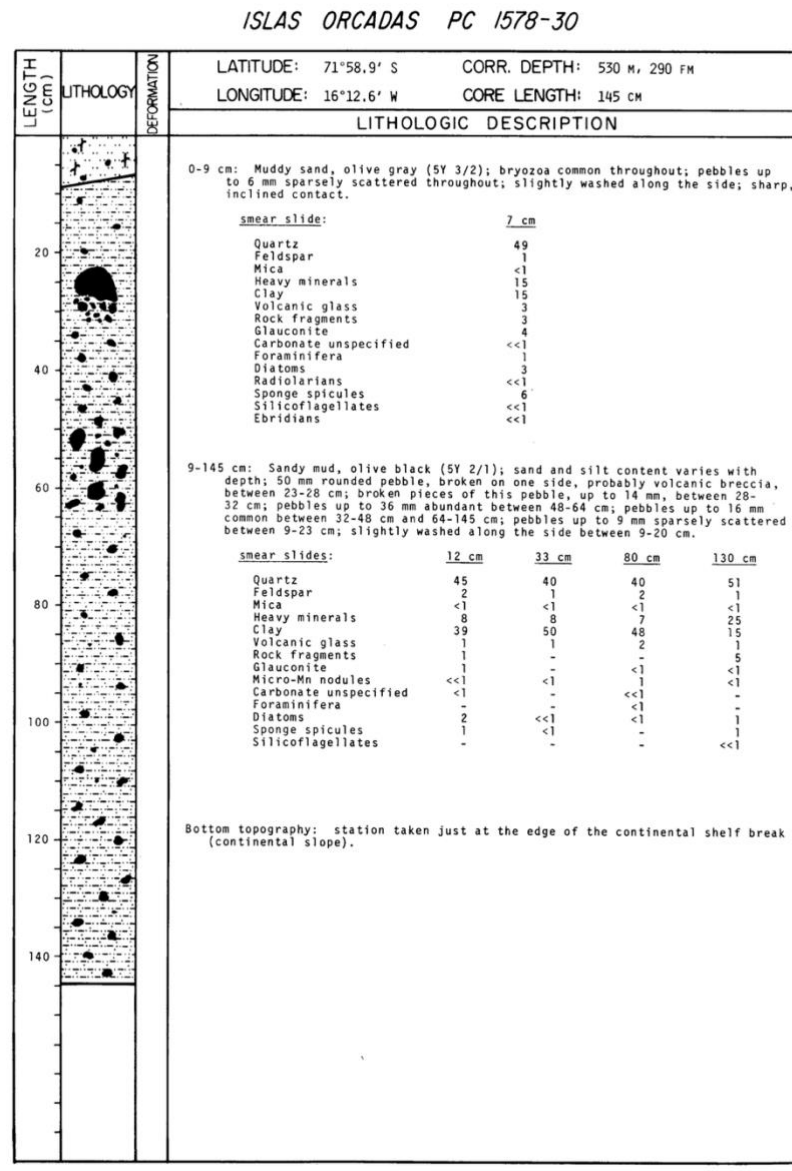
Loaded by: Watkins, Kaharoeddin, Graves, Bergen

Logged by: Watkins, Kaharoeddin, Graves, Bergen

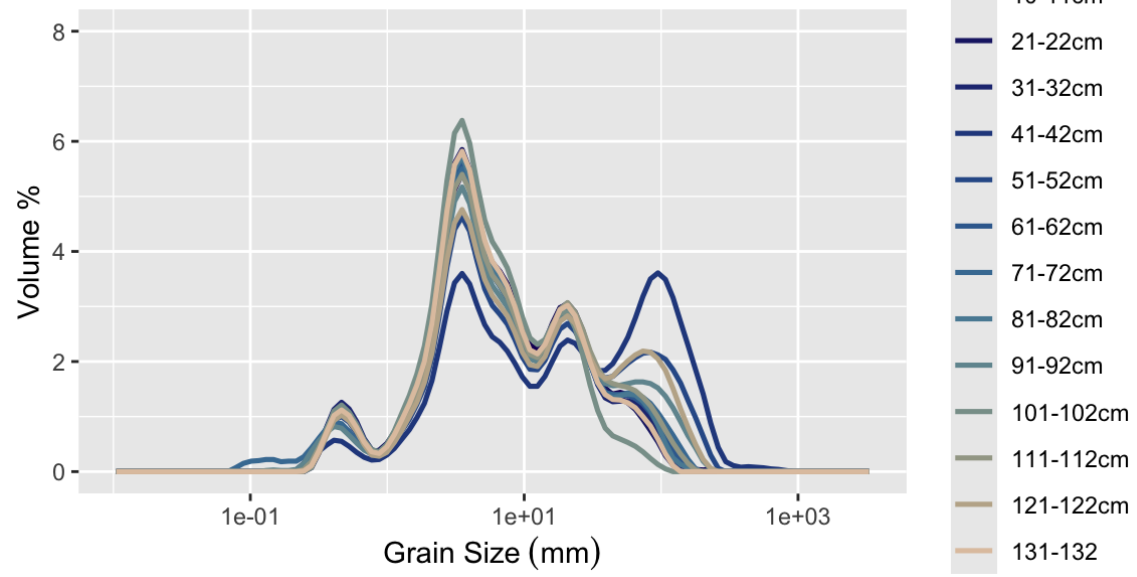
CRUISE: IO1578 CORE_ID: 26 TYPE: PC



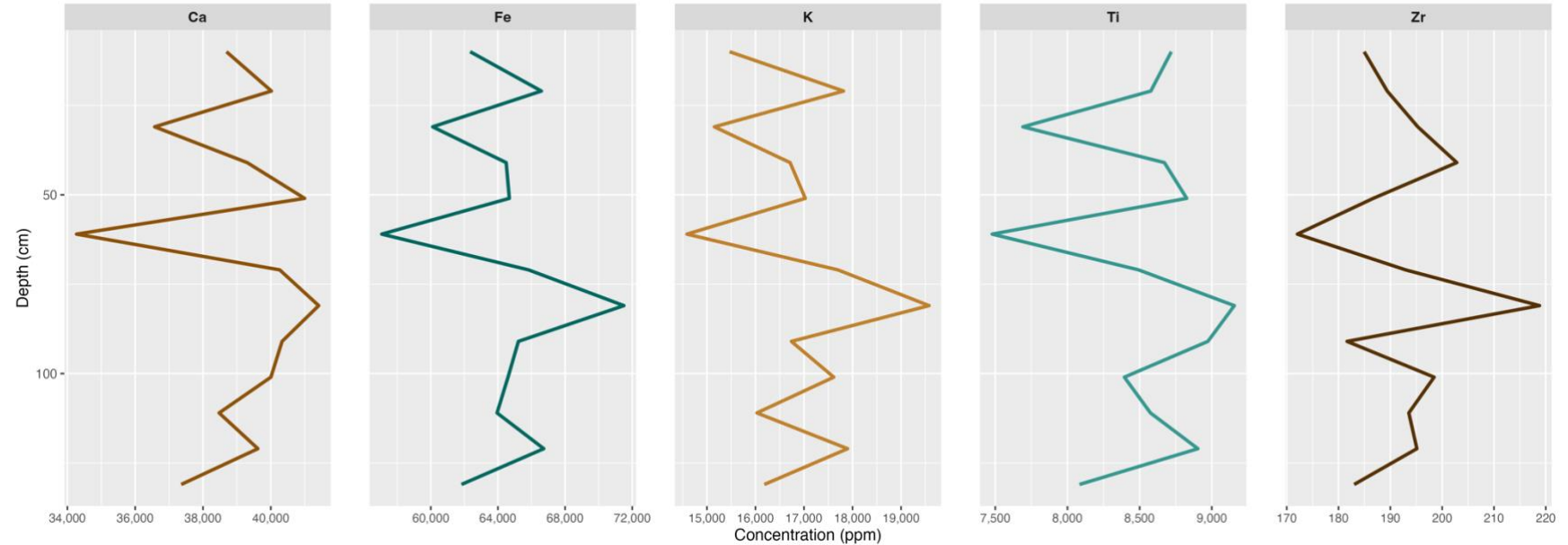
CRUISE: IO1578 CORE_ID: 30 TYPE: PC



Grain Size IO1578_30_PC

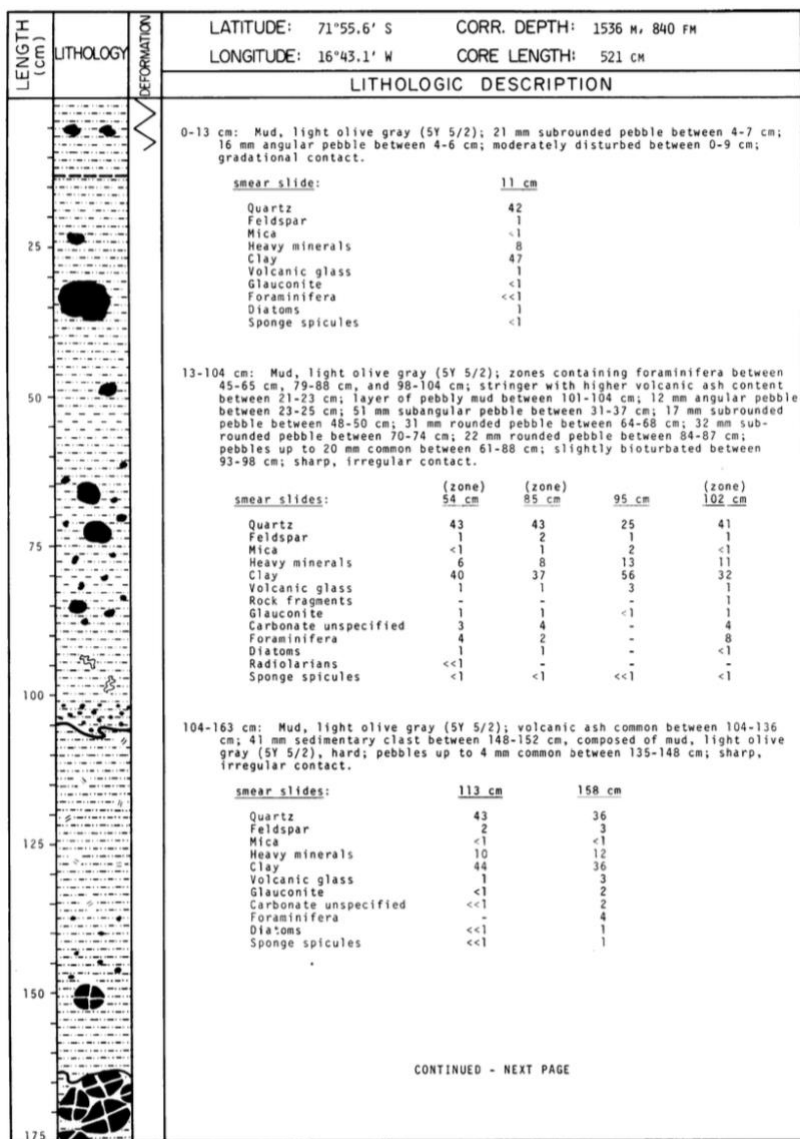


XRF IO1578_30_PC



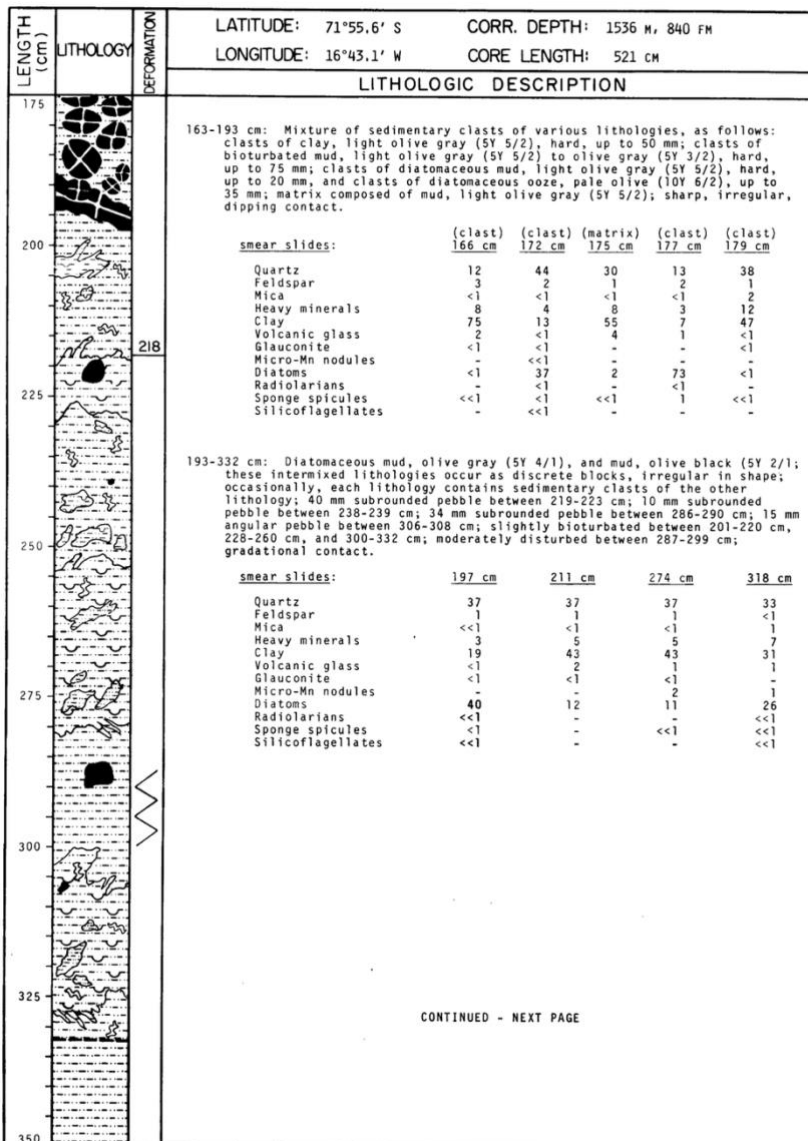
CRUISE: IO1578 CORE_ID: 33 TYPE: PC

ISLAS ORCADAS PC 1578-33



Logged by: Watkins, Bergen, Graves, Eggers

ISLAS ORCADAS PC 1578-33



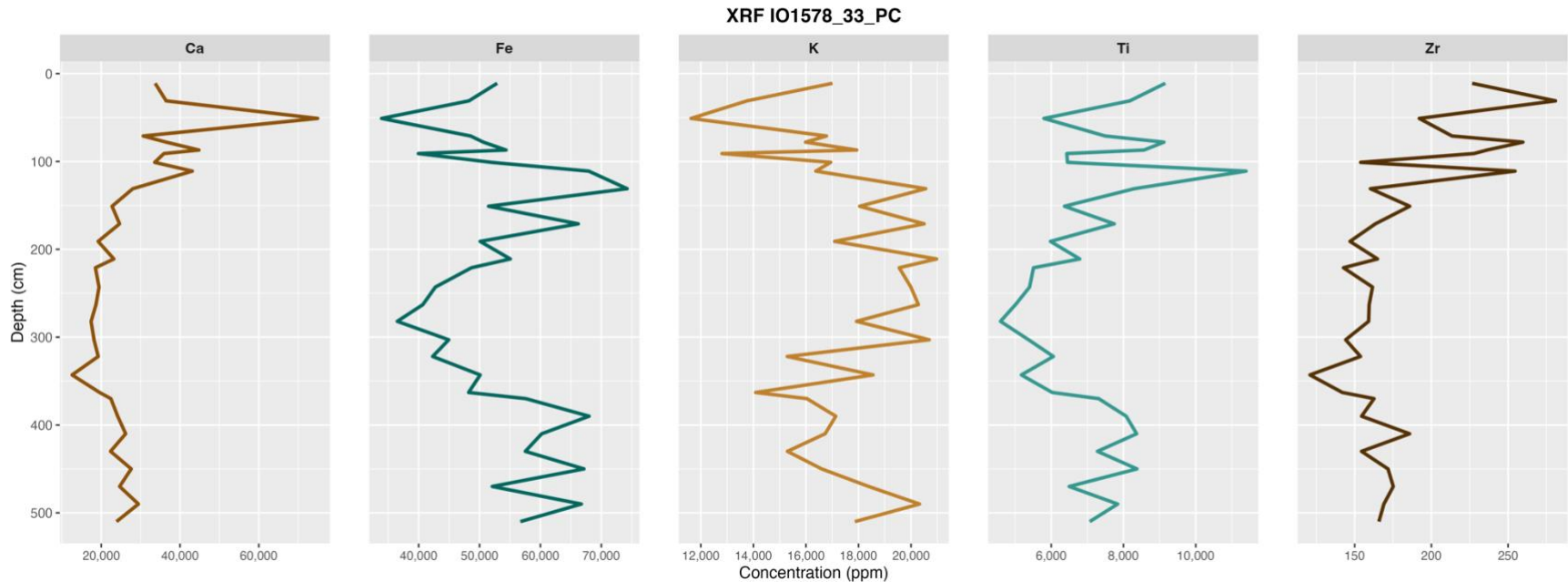
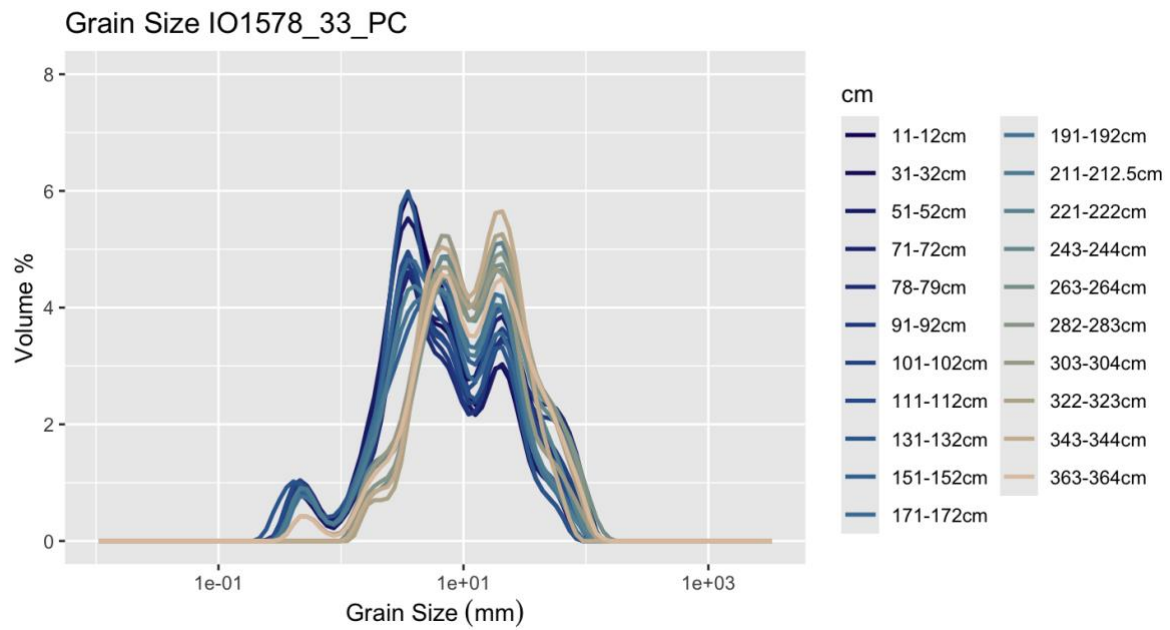
Logged by: Watkins, Bergen, Graves, Eggers

ISLAS ORCADAS PC 1578-33

LENGTH (cm)	LITHOLOGY	DEFORMATION	LATITUDE: 71°55.6' S	CORR. DEPTH: 1536 M, 840 FM
			LONGITUDE: 16°43.1' W	CORE LENGTH: 521 CM
LITHOLOGIC DESCRIPTION				
350			332-392 cm: Mud, olive black (5Y 2/1); sedimentary clast between 366-369 cm, composed of diatomaceous ooze, yellowish gray (5Y 7/2), hard; gradational contact.	
			<u>smear slide:</u> 379 cm	
			Quartz 32	
			Feldspar <1	
			Mica <1	
			Heavy minerals 10	
			Clay 53	
			Volcanic glass 1	
			Glauconite 4	
			Diatoms <1	
			Sponge spicules <1	
			Silicoflagellates <<1	
375				
392			392-440 cm: Diatomaceous mud, olive black (5Y 2/1); gradational contact.	
			<u>smear slide:</u> 425 cm	
			Quartz 33	
			Feldspar 1	
			Mica <1	
			Heavy minerals 11	
			Clay 29	
			Volcanic glass <1	
			Glauconite <<1	
			Diatoms 26	
			Radiolarians <<1	
			Sponge spicules <<1	
			Silicoflagellates <1	
400				
425			440-521 cm: Mud, olive black (5Y 2/1); zone of higher diatom content between 473-478 cm; 20 mm sedimentary clast between 468-470 cm, composed of clay, grayish olive (10Y 4/2), hard; 5 mm sedimentary clast between 477-478 cm, composed of clay, grayish olive (10Y 4/2), hard; highly disturbed between 499-521 cm.	
			<u>smear slide:</u> 481 cm	
			Quartz 48	
			Feldspar 2	
			Mica <1	
			Heavy minerals 15	
			Clay 30	
			Volcanic glass 3	
			Glauconite 2	
			Diatoms <<1	
			Sponge spicules <<1	
450				
475			Bottom topography: cored on the Antarctic continental slope.	
500				
525				

Logged by: Watkins, Bergen, Graves, Eggers

CRUISE: IO1578 CORE_ID: 33 TYPE: PC



CRUISE: IO1578 CORE_ID: 35 TYPE: PC

ISLAS ORCADAS PC 1578-35

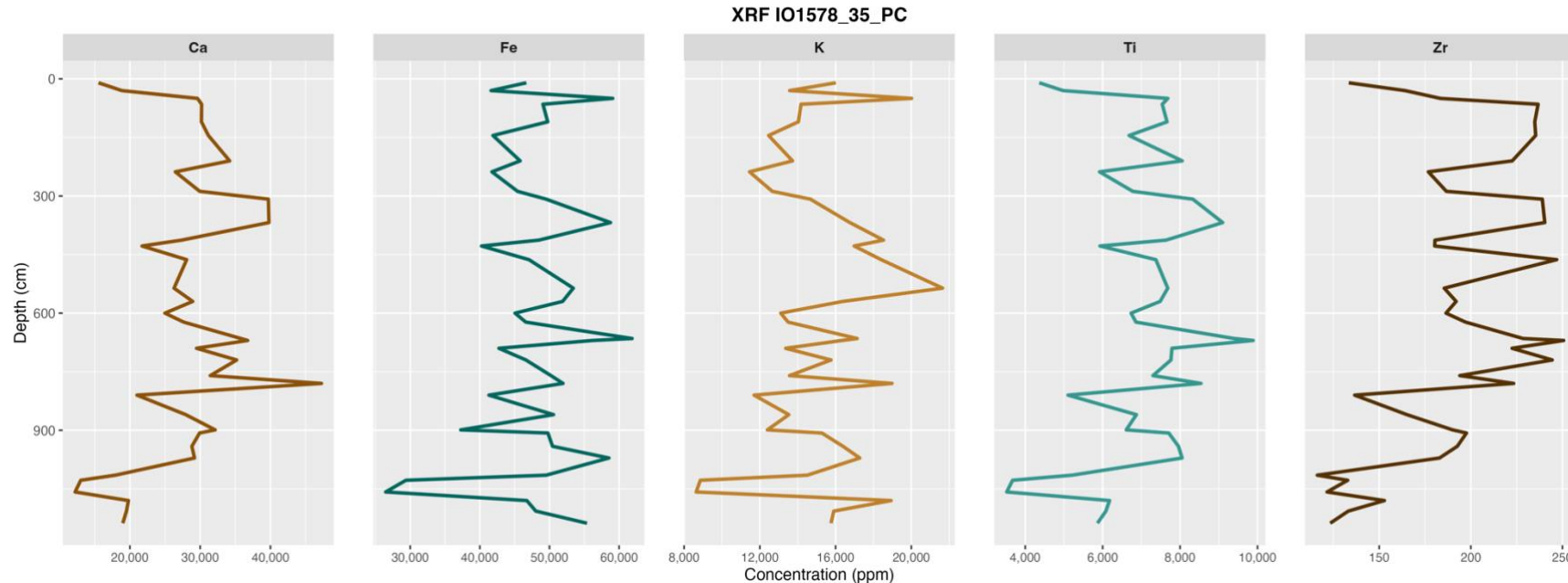
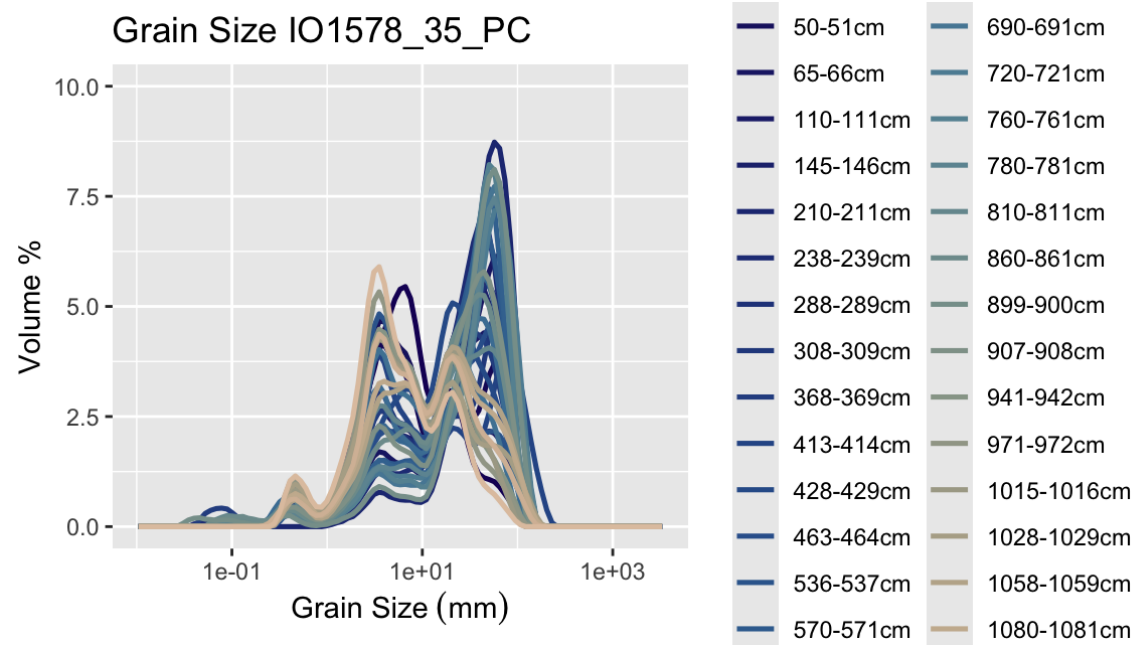
LENGTH (cm)	LITHOLOGY	DEFORMATION	LITHOLOGIC DESCRIPTION											
			LATITUDE: 71°51.5' S		CORR. DEPTH: 2350 M, 1285 FM		LONGITUDE: 17°10.2' W		CORE LENGTH: 1143 CM					
LITHOLOGIC DESCRIPTION														
0-59			0-59 cm: Mud, light olive gray (SY 5/2), gradationally changing to olive gray (SY 3/2) at 50 cm; three angular pebbles up to 11 mm between 48-50 cm; 5 mm angular pebble between 54-55 cm; slightly bioturbated between 45-54 cm; gradational contact.											
59-100			smear slides:	4 cm	42 cm		4 cm	42 cm						
100			Quartz	35	32	Glauconite	<1	<1						
			Feldspar	<1	1	Diatoms	10	<<1						
			Mica	<1	1	Radiolarians	<1	-						
			Heavy minerals	7	7	Sponge spicules	1	<1						
			Clay	45	57	Silicoflagellates	<<1	-						
			Volcanic glass	2	2	Ebridians	<<1	-						
100-200			59-366 cm: Mud, olive gray (SY 3/2); laminated with coarse silt, composed primarily of quartz particles, olive gray (SY 3/2); moderately laminated between 59-220 cm and between 252-347 cm; sparsely laminated between 220-252 cm and between 347-366 cm; slightly bioturbated between 220-252 cm; gradational contact.											
200			smear slides:	125 cm	275 cm		125 cm	275 cm						
			Quartz	48	43	Volcanic glass	1	<1						
			Feldspar	2	1	Glauconite	1	3						
			Mica	<1	1	Foraminifera	<1	<<1						
			Heavy minerals	10	12	Diatoms	-	<<1						
			Clay	38	40	Sponge spicules	<1	-						
200-292			366-480 cm: Mud, light olive gray (SY 5/2); zone of higher silt content between 415-421 cm; zone of higher diatom content between 421-431 cm; 15 mm angular pebble between 411-413 cm; 10 mm angular pebble between 414-415 cm; 18 mm subangular pebble between 427-429 cm; 1 cm lamina, higher in mud content, olive gray (SY 3/2), between 476-477 cm; gradational contact.											
292			smear slides:	384 cm	444 cm		384 cm	444 cm						
			Quartz	28	48	Glauconite	<<1	<1						
			Feldspar	1	2	Carbonate unspecified	<<1	<<1						
			Mica	<1	1	Foraminifera	<1	<<1						
			Heavy minerals	4	6	Diatoms	<1	8						
			Clay	67	34	Sponge spicules	<1	<1						
			Volcanic glass	<1	1									
292-400			480-695 cm: Mud, olive gray (SY 3/2); 0.2 cm laminae and stringers of very fine, silt size quartz particles between 566-574 cm and between 622-629 cm; highly laminated with laminae of silt size quartz particles between 664-690 cm; pebbles up to 3 mm sparsely scattered between 542-575 cm; 6 mm angular pebble between 664-665 cm; slightly bioturbated between 500-522 cm; gradational contact.											
400			smear slides:	512 cm	636 cm		512 cm	636 cm						
			Quartz	35	33	Volcanic glass	<1	2						
			Feldspar	2	2	Glauconite	1	1						
			Mica	<1	<1	Foraminifera	-	<1						
			Heavy minerals	9	7	Diatoms	<1	<<1						
			Clay	53	55	Sponge spicules	<1	<1						
400-534			534											
534			CONTINUED - NEXT PAGE											

Logged by: Kaharoeddin, Watkins, Graves, Bergen, Eggers

ISLAS ORCADAS PC 1578-35

LENGTH (cm)	LITHOLOGY	DEFORMATION	LITHOLOGIC DESCRIPTION												
			LATITUDE: 71°51.5' S		CORR. DEPTH: 2350 M, 1285 FM		LONGITUDE: 17°10.2' W		CORE LENGTH: 1143 CM						
LITHOLOGIC DESCRIPTION															
700			695-742 cm: Sandy mud, olive gray (SY 3/2); highly laminated with mud, olive gray (SY 3/2); between 710-722 cm, moderately laminated between 722-742 cm; 4 mm subangular pebble between 722-723 cm; sharp contact.												
700-837			smear slide:	727 cm											
837			Quartz	50		Rock fragments	<1								
			Feldspar	3		Glauconite	5								
			Mica	1		Carbonate unspecified	<1								
			Heavy minerals	17		Foraminifera	3								
			Clay	15		Diatoms	<1								
			Volcanic glass	5		Sponge spicules	1								
837-900			742-892 cm: Mud, olive gray (SY 3/2); highly laminated with laminae of fine, silt size quartz particles between 745-770 cm and between 875-892 cm; moderately laminated between 859-869 cm, slightly laminated between 804-859 cm; 7 mm subangular pebbles between 795-796 cm and 773-774 cm; slightly bioturbated between 790-804 cm; sharp contact.												
900			smear slides:	744 cm	873 cm		744 cm	873 cm							
			Quartz	50	48	Clay	37	38							
			Feldspar	2	1	Volcanic glass	<1	1							
			Mica	1	<1	Glauconite	1	<1							
			Heavy minerals	9	12	Diatoms	-	<<1							
900-1000			892-919 cm: Mud, olive gray (SY 4/1); moderately laminated with very fine, silt size quartz particles between 892-909 cm; laminae contain foraminifera between 893-894 cm; 10 mm subangular pebble between 892-893 cm; 4 mm angular pebble between 907-908 cm; slightly bioturbated lamina of clay, light olive gray (SY 5/2), between 907-908 cm; gradational contact.												
1000			smear slide:	899 cm											
			Quartz	39		Volcanic glass	2								
			Feldspar	2		Glauconite	1								
			Mica	1		Diatoms	<<1								
			Heavy minerals	8		Sponge spicules	<1								
			Clay	48											
1000-1143			919-1143 cm: Mud, olive gray (SY 3/2); coarse quartz sand abundant throughout; coarse pebbles common (about every 40 cm); fine and medium pebbles sparsely scattered throughout; 20 mm sedimentary clasts, of various shapes and composed of mud and muddy, diatomaceous ooze, common throughout; 12 cm long sedimentary clast between 1077-1089 cm composed of diatomaceous ooze.												
1143			smear slides:	1002 cm	1069 cm	1084 cm	1002 cm	1069 cm	1084 cm	1135 cm					
			Quartz	34	53	17	53	17	45						
			Feldspar	2	2	2	2	2	2						
			Mica	<1	<1	<1	<1	<1	<1						
			Heavy minerals	10	5	2	5	2	8						
			Clay	40	38	12	38	12	31						
			Volcanic glass	2	1	64	1	64	6						
			Glauconite	<1	<1	2	<1	<1	2						
			Diatoms	12	1	2	1	2	3						
			Radiolarians	<1	-	1	-	1	1						
			Sponge spicules	<1	<1	1	<1	1	1						
			Silicoflagellates	<<1	-	<<1	-	<<1	<<1						
Bottom topography: cored on the Antarctic continental slope.															

Logged by: Kaharoeddin, Watkins, Graves, Bergen, Eggers



CRUISE: IO1578 CORE_ID: 38 TYPE: PC

ISLAS ORCADAS PC 1578-38

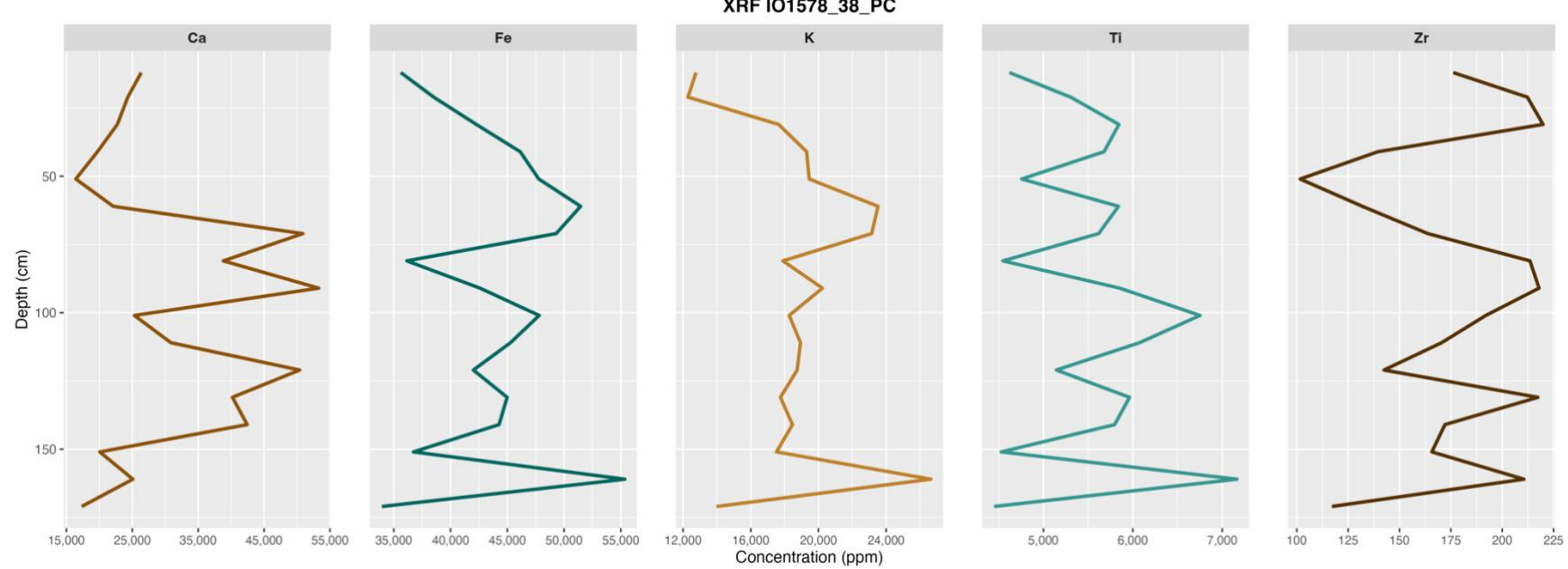
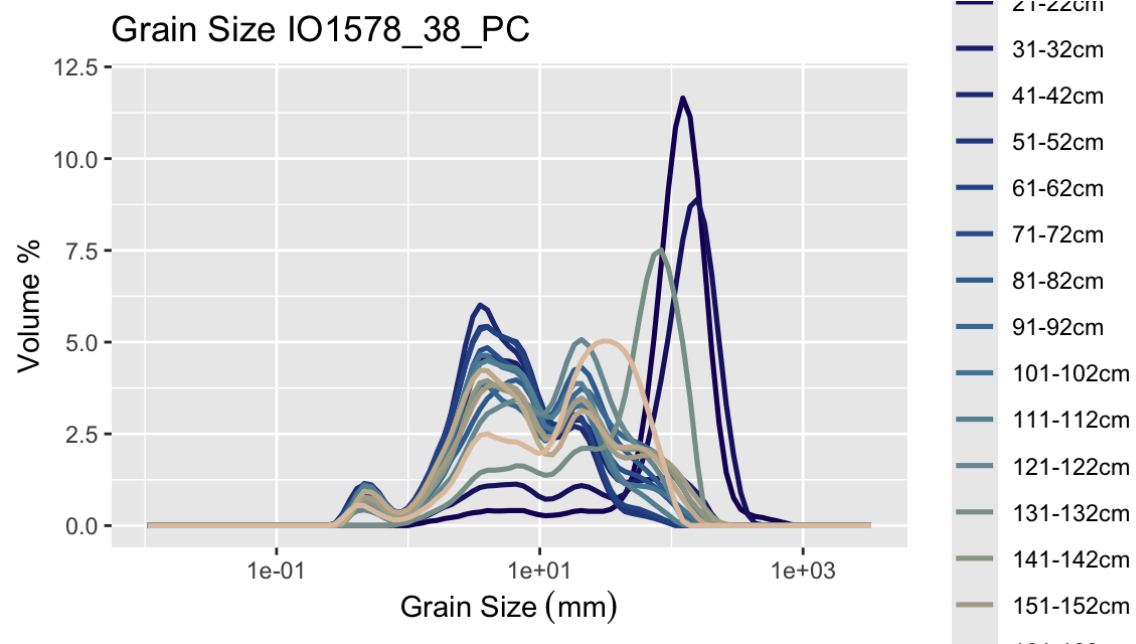
LENGTH (cm)	LITHOLOGY	DEFORMATION	LATITUDE: 71°14.2' S	WATER DEPTH: 4301 m, 2352 FM
			LONGITUDE: 19°08.8' W	CORE LENGTH: 486 CM
LITHOLOGIC DESCRIPTION				
0-26			0-26 cm: Sand, olive gray (5Y 3/2), moderately well-sorted, grain size increases with depth from a very fine to fine sand; foraminifera present, content increasing slightly with depth; slightly washed along the side; sharp, inclined, irregular contact.	
26			<u>smear slide:</u> 2 cm	
			Quartz 72 Feldspar 3 Mica <1 Heavy minerals 17 Clay <1 Volcanic glass 2 Glauconite 5 Carbonate unspecified <1 Foraminifera 1 Sponge spicules <1	
26-178			26-178 cm: Mud, light olive gray (5Y 5/2); foraminifera present between 62-91 cm and 108-148 cm; layer of sand between 143-145 cm, olive gray (5Y 3/2), containing foraminifera, with sharp and irregular contacts; lenses of sand up to 1.2 cm thick between 43-49 cm, 104-107 cm, 128-130 cm, and 145-147 cm, olive gray (5Y 3/2), all containing foraminifera; stringers of mud common between 51-52 cm, rich in volcanic ash, olive gray (5Y 4/1); abundant stringers between 172-178 cm, composed of silt to very fine sand, light olive gray (5Y 5/2); slightly washed along the side; sharp, curved contact.	
178			<u>smear slides:</u> 52 cm 118 cm 172 cm	
			Quartz 27 40 46 Feldspar 1 2 2 Mica <1 <1 <1 Heavy minerals 8 11 12 Clay 63 18 36 Volcanic glass <1 3 3 Glauconite <1 4 1 Carbonate unspecified 1 12 - Foraminifera <1 10 - Calcareous nannos <1 - - Diatoms <1 - - Sponge spicules <1 <1 <1	
178-184			178-184 cm: Medium sand, olive gray (5Y 3/2); moderately sorted; foraminifera present; slightly washed along the side; sharp, irregular contact.	
184-199			184-199 cm: Muddy sand, light olive gray (5Y 5/2); coarse fraction consisting of well-sorted, fine sand; core sediment separated between 190-192 cm, with sediment from the overlying sand unit filling this crack, and present in the wash along the side; slightly washed along the side; sharp contact.	
199			<u>smear slide:</u> 197 cm	
			Quartz 50 Feldspar 1 Mica <1 Heavy minerals 9 Clay 22 Volcanic glass 5 Glauconite 3 Carbonate unspecified 4 Foraminifera 6 Sponge spicules <1	
CONTINUED - NEXT PAGE				

Logged by: Bergen, Eggers, Graves

ISLAS ORCADAS PC 1578-38

LENGTH (cm)	LITHOLOGY	DEFORMATION	LATITUDE: 71°14.2' S	WATER DEPTH: 4301 m, 2352 FM
			LONGITUDE: 19°08.8' W	CORE LENGTH: 486 CM
LITHOLOGIC DESCRIPTION				
350			350-486 cm: Pebbles, olive gray (5Y 3/2); very fine-grained pebbles are dominant throughout; increase in the number of large pebbles with depth; layer of sand between 199-217 cm, olive gray (5Y 3/2), composed of medium to coarse sand with grain size increasing with depth, grading into pebble unit; much larger pebbles, subangular to subrounded, between 352-356 cm (32 mm), 365-368 cm (27 mm) 402-405 cm (28 mm) and 415-419 cm (21 mm).	
400				
450				Bottom topography: abyssal plain.
500				

Logged by: Bergen, Eggers, Graves

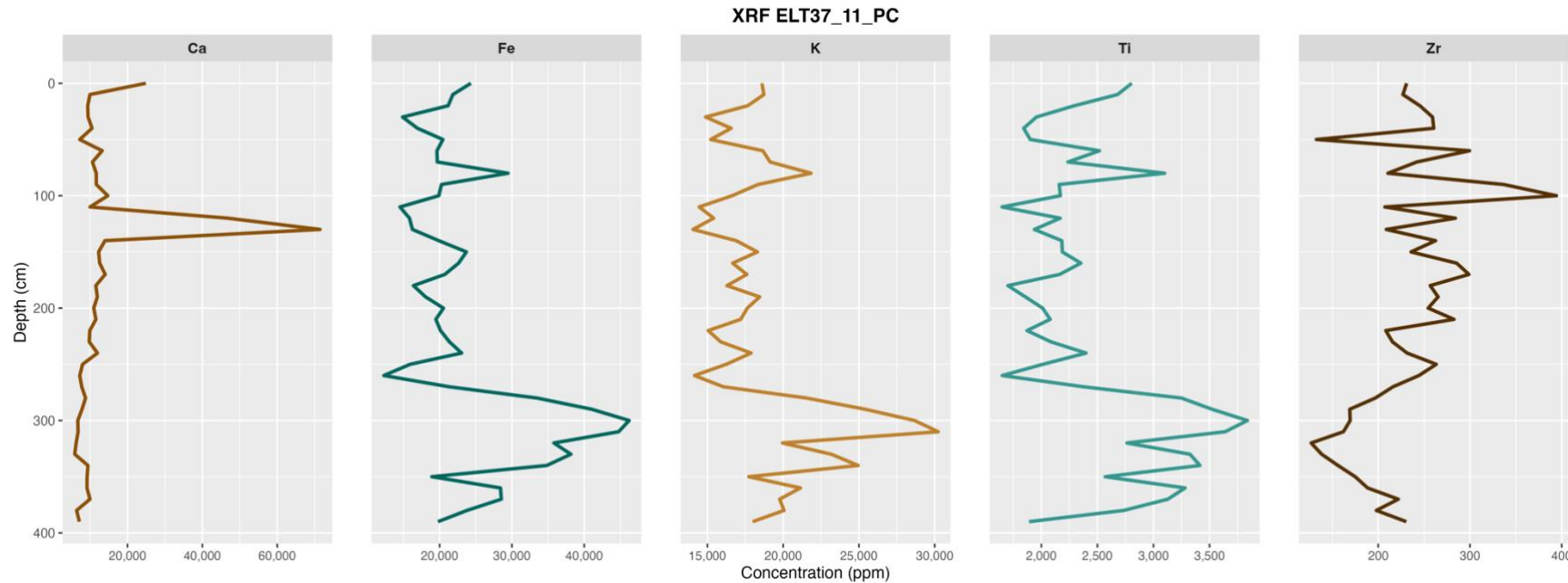
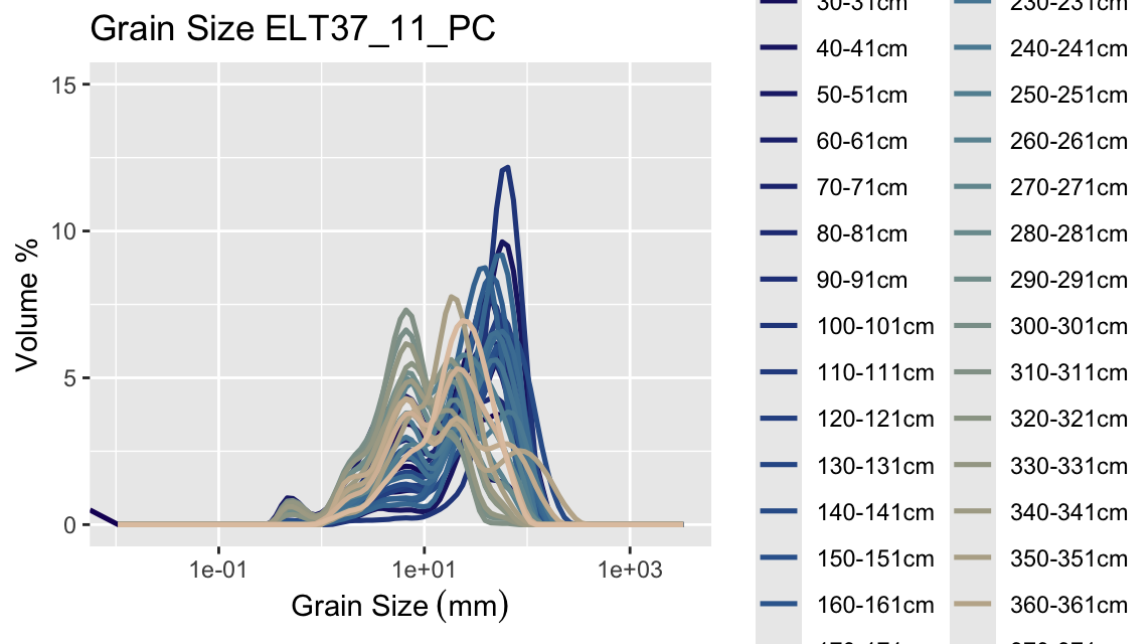


Pennell Coast / George V Land Cores

CRUISE: ELTANIN CORE ID: 37-11 TYPE: PC

USNS ELTANIN				
CORE PC 37-11				
		LATITUDE 64-31.2 S	LONGITUDE 138-00.0 E	WATER DEPTH 1705 F
DEPTH (CM)	COLOR	LITHOLOGY	REMARKS	
0-29	SY5/2	MUD, SANDY, SPINES	WASHED, SHARP BASE, ABUND. HVY MIN..	
29-47	SY4/2	MUD, SANDY, SPINES	SHARP BASE, ABUND. HVY MIN., LAMINATED.	
47-59	SY5/2	MUD, SANDY	SHARP BASE.	
59-173	SY6/2, SY3/2	MUD, SANDY, FORAM., SPINES	GRADATIONAL BASE, MOTTLING, MN NODULES, MN MICRONODULES, LAMINATED.	
173-175	SY6/2	SAND, FORAM., SPINES	GRADATIONAL BASE, MN NODULES.	
175-189	SY5/2, SY4/2	MUD, SANDY, FORAM., SPINES	GRADATIONAL BASE, MOTTLING, MN NODULES, MN MICRONODULES, ABUND. HVY MIN..	
189-207	SY5/2, SY4/2	MUD, SANDY, SPINES	GRADATIONAL BASE, LAMINATED.	
207-234	10SY5/2	MUD, SANDY, SPINES	SECTION MISSING, GRADATIONAL BASE, MN NODULES, MN MICRONODULES, LAMINATED.	
234-252	10SY5/4	MUD, SANDY, SPINES, RADIGLAR.	GRADATIONAL BASE, MN MICRONODULES.	
252-255	SY6/4	MUD, SANDY, DIATOM., SPINES	CORE DESICCATED, SHARP BASE.	
255-277	SY6/4, 50SY5/2	MUD, SANDY	SHARP BASE, MN NODULES, MN MICRONODULES, LAMINATED.	
277-405	10SY5/2	MUD, SANDY	SHARP BASE.	
405-417	10SY4/4	MUD, SANDY, DIATOM., SPINES	SUCKED, GAP IN CORE.	

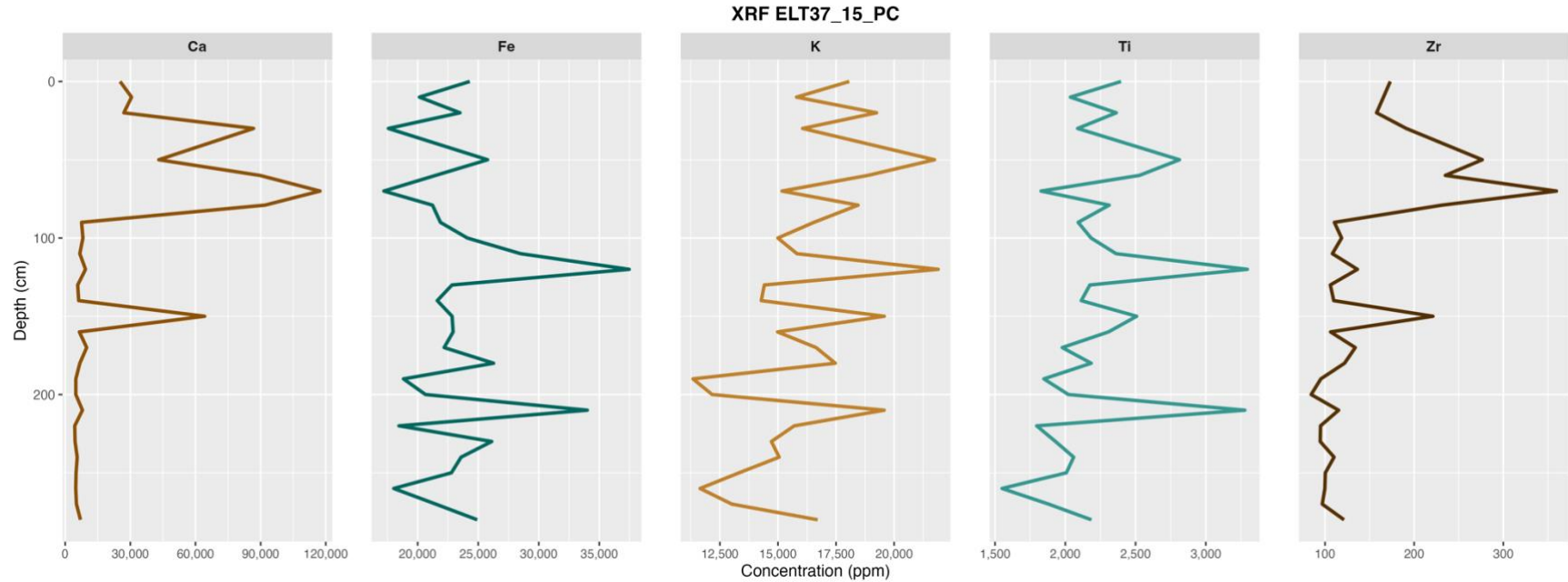
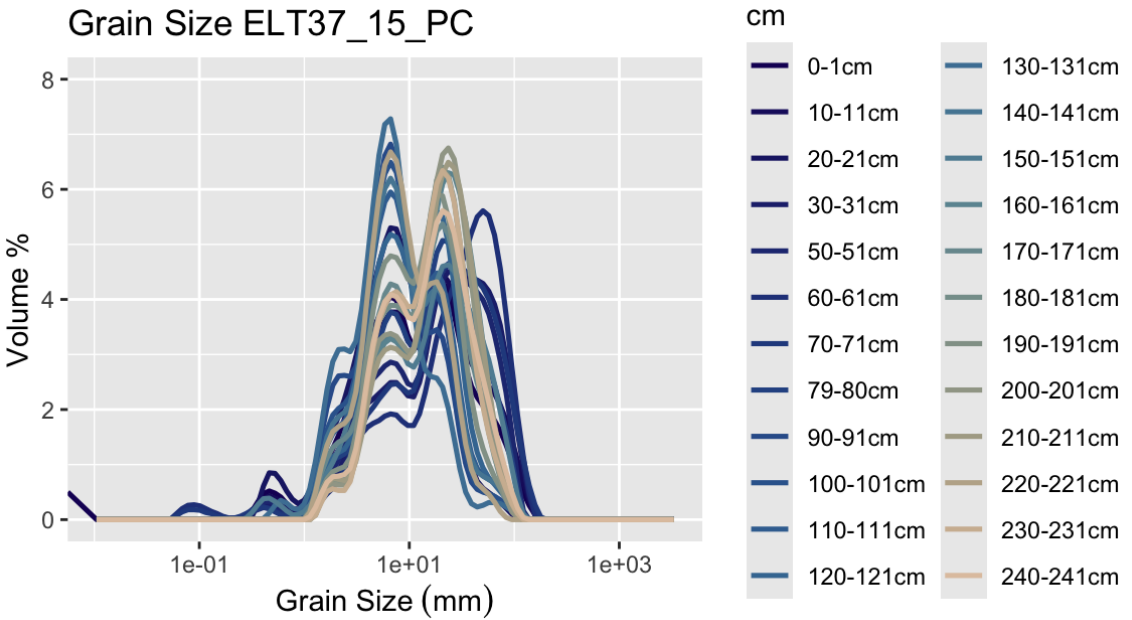
CRUISE: ELTANIN CORE_ID: 37-11 TYPE: PC



CRUISE: ELTANIN CORE_ID: 37-15 TYPE: PC

USNS ELTANIN
CORE PC 37-15

DEPTH(CM)	COLOR	LITHOLOGY	REMARKS
0-70	10YR5/2	MUD, FORAM., SANDY	GRADATIONAL BASE, ISOLATED PEBBLES.
70-89	10YR6/2	MUD, SANDY, DIATOM., SPICULES	CALCAREOUS, GRADATIONAL BASE.
89-182	10YR5/4, 10YR5/6	MUD	CALCAREOUS, SHARP BASE, HOTTLING.
182-209	10YR5/2	MUD	CALCAREOUS, SHARP BASE.
209-229	10YR5/4	MUD	CALCAREOUS, SHARP BASE.
229-282	10YR6/4, 10YR5/6	MUD, SANDY, SPICULES	CALCAREOUS, HOTTLING, ABUND. HVY MIN..



Core	Top	Record	D50 (um)	D100	Sorting	Skewness	Mean	Eccentrici	Mean	Circuluari	MS	Ca (ppm)	K (ppm)	Ti (ppm)	Zr (ppm)	Fe (ppm)
	depth (cm)	number	(um)				eccentrici	ty SD	circularity	ty SD	5 SI)					
IO1578_30_PC	10	1	6.0	237.2	1.92	0.13	0.414	0.169	0.650	0.055	164.623	162	15467	8720	185	62348
IO1578_30_PC	21	2	5.5	124.9	1.82	0.15	0.423	0.169	0.649	0.057	527.755	165	17815	8578	189	66592
IO1578_30_PC	31	3	5.5	161.3	1.90	0.14	0.415	0.170	0.651	0.049	135.795	151	15153	7691	195	60111
IO1578_30_PC	41	4	9.4	241.0	2.23	0.12	0.429	0.183	0.627	0.056	310.447	161	16714	8672	203	64492
IO1578_30_PC	51	5	8.4	273.9	2.33	0.15	0.429	0.177	0.627	0.055	211.842	165	17027	8826	187	64680
IO1578_30_PC	61	6	5.7	162.2	1.93	0.15	0.430	0.167	0.625	0.057	11.068	145	14588	7478	172	57077
IO1578_30_PC	71	7	5.7	183.8	2.05	0.14	0.393	0.179	0.632	0.051	294.307	162	17698	8493	193	65825
IO1578_30_PC	81	8	5.5	161.7	1.92	0.16	0.402	0.173	0.636	0.056	288.557	171	19578	9156	219	71508
IO1578_30_PC	91	9	6.8	238.8	2.10	0.18	0.431	0.155	0.626	0.063	209.398	164	16740	8973	182	65221
IO1578_30_PC	101	10	4.7	108.2	1.64	0.10	0.401	0.172	0.628	0.053	938.232	162	17614	8394	198	64603
IO1578_30_PC	111	11	6.1	181.8	1.96	0.14	0.413	0.169	0.632	0.056	520.15	159	16030	8575	194	63948
IO1578_30_PC	121	12	7.8	239.8	2.22	0.15	0.423	0.157	0.623	0.064	510.099	165	17899	8904	195	66732
IO1578_30_PC	131	13	5.4	124.8	1.84	0.15	0.411	0.169	0.637	0.053	449.253	155	16182	8083	183	61829
IO1578_19_PC	11	14	10.1	123.2	1.36	0.07	0.443	0.166	0.634	0.056	44.534	21962	22198	6460	215	52145
IO1578_19_PC	30	15	12.6	159.1	1.74	-0.04	0.439	0.164	0.631	0.051	62.719	22131	18369	6230	206	38344
IO1578_19_PC	56	16	11.8	160.8	1.70	-0.02	0.424	0.180	0.641	0.047	79.121	22271	18172	6088	182	39311
IO1578_19_PC	70	17	7.5	124.4	1.79	0.07	0.431	0.174	0.645	0.044	200.998	24677	19964	7086	163	45906
IO1578_19_PC	90	18	6.1	107.4	1.57	0.08	0.458	0.175	0.638	0.066	204.039	24881	16586	7263	157	57163
IO1578_19_PC	110	19	5.8	83.0	1.53	0.09	0.464	0.182	0.636	0.063	56.367	29230	15863	7554	164	54130
IO1578_19_PC	130	20	13.9	241.8	2.16	0.05	0.432	0.172	0.625	0.055	130.634	29474	19800	9472	238	54904
IO1578_19_PC	150	21	68.4	278.6	1.85	-0.49	0.428	0.167	0.620	0.055	197.16	23497	15072	7453	212	46961
IO1578_19_PC	170	22	7.7	142.4	1.88	0.08	0.430	0.159	0.627	0.058	198.351	33769	18766	9719	244	58507
IO1578_19_PC	190	23	7.8	157.4	1.74	0.12	0.425	0.183	0.634	0.056	226.786	35473	16058	6769	164	56500
IO1578_19_PC	210	24	9.2	142.0	1.88	0.05	0.460	0.167	0.630	0.055	314.211	39823	17063	7382	187	49268
IO1578_19_PC	230	25	36.0	243.1	2.26	-0.38	0.422	0.168	0.624	0.051	78.584	39973	19629	7557	249	43708
IO1578_19_PC	250	26	8.6	123.9	1.58	0.07	0.432	0.167	0.633	0.055	86.983	29552	16521	9714	246	51559
IO1578_19_PC	270	27	7.8	107.9	1.56	0.05	0.419	0.166	0.632	0.058	62.453	31317	16411	7711	174	55200
IO1578_19_PC	290	28	7.2	122.7	1.62	0.09	0.424	0.173	0.630	0.050	53.455	31270	17016	8344	187	57765
IO1578_19_PC	310	29	16.1	162.4	1.93	-0.15	0.403	0.178	0.645	0.045	120.845	36382	17577	10221	275	57383
IO1578_19_PC	330	30	5.6	94.2	1.47	0.11	0.448	0.170	0.639	0.053	221.099	23194	16201	5330	136	56560
IO1578_19_PC	350	31	14.0	162.8	1.95	-0.08	0.423	0.177	0.646	0.043	294.243	34299	16696	10545	219	55610
IO1578_19_PC	370	32	10.2	162.9	1.94	0.04	0.393	0.185	0.637	0.054	172.558	31119	16621	8064	206	53984
IO1578_19_PC	380	33	10.7	124.6	1.84	-0.04	0.428	0.188	0.644	0.043	201.531	31886	16767	7787	179	53739
IO1578_19_PC	390	34	11.7	160.8	1.88	-0.02	0.414	0.159	0.638	0.050	154.242	33194	16229	8953	265	55155
IO1578_19_PC	410	35	16.3	186.1	1.98	-0.08	0.415	0.174	0.641	0.046	234.927	33625	16288	8654	216	54235
IO1578_19_PC	430	36	7.3	107.9	1.66	0.04	0.435	0.173	0.637	0.055	216.475	31468	15963	8124	194	53172
IO1578_19_PC	450	37	11.4	124.8	1.83	-0.06	0.410	0.178	0.645	0.048	222.561	32459	15218	8246	191	52151
IO1578_19_PC	470	38	9.8	142.5	1.89	0.04	0.416	0.167	0.647	0.043	406.004	37649	17570	10061	306	54725
IO1578_19_PC	490	39	26.0	163.0	1.90	-0.34	0.419	0.171	0.646	0.042	NaN	33675	14578	8594	255	46548
IO1578_26_PC	20	40	8.0	124.7	1.89	0.12	0.436	0.174	0.652	0.038	NaN	30395	20601	8309	206	60370
IO1578_26_PC	30	41	6.0	124.8	1.91	0.21	0.421	0.177	0.643	0.051	NaN	31515	21488	8864	198	64382
IO1578_26_PC	40	42	6.0	123.2	1.77	0.19	0.423	0.185	0.642	0.054	NaN	27001	21887	7992	184	65464
IO1578_26_PC	50	43	8.7	109.4	1.76	0.02	0.412	0.177	0.649	0.039	NaN	33778	18875	8954	209	62220
IO1578_26_PC	60	44	16.7	123.2	1.84	-0.32	0.439	0.161	0.651	0.041	NaN	34796	19939	9389	257	67112
IO1578_26_PC	80	45	15.2	123.2	1.86	-0.25	0.444	0.189	0.642	0.048	134.935	31826	16678	8178	205	56013
IO1578_26_PC	90	46	23.9	125.3	1.77	-0.34	0.408	0.180	0.654	0.047	209.732	15030	10670	4170	124	36006
IO1578_26_PC	100	47	6.0	95.6	1.77	0.08	0.432	0.165	0.662	0.042	109.999	22493	16745	6704	148	56171
IO1578_26_PC	110	48	12.1	108.9	1.76	-0.13	0.427	0.171	0.655	0.047	134.538	35642	17720	8615	190	62261
IO1578_26_PC	120	49	13.3	109.1	1.85	-0.22	0.443	0.184	0.651	0.048	75.548	37595	18492	9134	221	61912
IO1578_26_PC	130	50	16.8	120.6	1.83	-0.32	0.405	0.164	0.657	0.040	155.958	38804	17723	8465	227	57517
IO1578_26_PC	140	51	10.0	108.4	1.72	-0.04	0.439	0.164	0.652	0.040	NaN	34942	17301	8735	199	60926
IO1578_26_PC	150	52	13.2	139.3	1.95	-0.15	0.414	0.161	0.649	0.043	94.855	37493	16321	8802	232	54087
IO1578_26_PC	160	53	14.0	124.9	1.96	-0.18	0.395	0.176	0.652	0.035	228.043	38772	17504	8387	228	54824
IO1578_26_PC	170	54	13.5	124.8	1.86	-0.15	0.408	0.157	0.650	0.049	276.716	39095	16564	8436	243	53078
IO1578_26_PC	180	55	21.6	125.1	1.81	-0.33	0.429	0.153	0.651	0.036	151.928	39020	17339	9286	226	58255
IO1578_26_PC	190	56	15.3	109.0	1.75	-0.28	0.427	0.190	0.657	0.041	151.727	41663	17327	9595	245	59089
IO1578_26_PC	200	57	14.2	124.6	1.96	-0.23	0.426	0.172	0.658	0.046	242.065	40886	17449	9945	217	61489
IO1578_26_PC	210	58	14.2	109.2	1.84	-0.23	0.437	0.160	0.656	0.038	116.549	30249	19314	7439	162	64181
IO1578_26_PC	220	59	19.1	125.1	1.87	-0.29	0.432	0.170	0.648	0.050	79.841	40250	17211	9265	240	59614
IO1578_26_PC	250	60	11.0	108.8	1.74	-0.11	0.052	0.188	0.646	0.052	205.494	38612	18074	8897	205	63432
IO1578_26_PC	280	61	20.4	109.2	1.68	-0.38	0.441	0.171	0.657	0.032	261.836	43011	17361	10147	230	59245
IO1578_26_PC	310	62	4.9	106.7	1.69	0.11	0.446	0.190	0.652	0.052	37.063	39100	23949	8020	191	64234
IO1578_26_PC	340	63	14.7	163.0	2.08	-0.11	0.460	0.163	0.649	0.046	69.132	22783	23556	4986	100	55063
IO1578_26_PC	370	64	7.3	108.6	1.90	0.02	0.409	0.184	0.652	0.047	NaN	25349	17088	7593	168	57558
IO1578_26_PC	400	65	5.7													

IO1578_26_PC	770	77	22.1	109.3	1.80	-0.44	0.436	0.167	0.659	0.034	322.746	28745	14069	6431	177	47990
IO1578_26_PC	800	78	26.8	183.0	1.99	-0.39	0.429	0.179	0.648	0.040	128.056	20507	16476	5468	161	40013
IO1578_26_PC	830	79	5.5	123.6	1.89	0.14	0.444	0.168	0.654	0.041	93.798	16026	24078	5728	115	53529
IO1578_26_PC	860	80	12.7	124.5	1.88	-0.14	0.430	0.176	0.656	0.048	196.241	32656	20326	8798	198	66291
IO1578_26_PC	890	81	18.5	124.3	1.79	-0.30	0.421	0.169	0.651	0.043	226.786	32642	16859	8533	216	54441
IO1578_26_PC	920	82	11.7	109.0	1.85	-0.17	0.407	0.184	0.648	0.049	263.166	38647	16417	9008	212	58678
IO1578_26_PC	950	83	10.6	124.5	1.83	-0.05	0.411	0.170	0.652	0.047	218.392	35379	18109	9644	247	56648
IO1578_33_PC	11	84	5.1	83.0	1.61	0.09	0.421	0.171	0.645	0.060	29.124	33676	17010	9159	227	52898
IO1578_33_PC	31	85	7.9	108.6	1.70	0.03	0.405	0.174	0.651	0.051	128.054	36475	13758	8176	281	48256
IO1578_33_PC	51	86	5.2	106.7	1.69	0.10	0.453	0.183	0.637	0.064	271.759	74942	11627	5798	192	33914
IO1578_33_PC	71	87	7.4	122.7	1.78	0.01	0.460	0.168	0.629	0.063	NaN	30630	16783	7495	213	48530
IO1578_33_PC	78	88	8.0	124.8	1.98	0.04	0.433	0.167	0.637	0.058	189.422	36472	15985	9120	260	50630
IO1578_33_PC	87	89	7.2	141.2	1.87	0.08	0.442	0.176	0.646	0.048	199.151	44804	17935	8568	236	54361
IO1578_33_PC	91	90	7.5	125.1	1.91	0.09	0.417	0.174	0.649	0.046	195.182	35911	12803	6431	228	39953
IO1578_33_PC	101	91	6.9	123.9	1.84	0.06	0.427	0.187	0.650	0.054	NaN	33551	16941	6450	154	51956
IO1578_33_PC	111	92	7.0	107.4	1.77	0.01	0.448	0.174	0.641	0.057	9.349	43125	16373	11393	255	67932
IO1578_33_PC	131	93	5.1	83.0	1.70	0.07	0.447	0.185	0.635	0.069	67.478	28009	20560	8300	160	74242
IO1578_33_PC	151	94	7.7	108.4	1.65	0.02	0.442	0.181	0.646	0.057	NaN	22738	18041	6365	186	51473
IO1578_33_PC	171	95	6.4	107.4	1.63	0.07	0.437	0.175	0.635	0.073	134.4	24649	20499	7745	164	66221
IO1578_33_PC	191	96	7.4	94.6	1.55	-0.01	0.475	0.170	0.629	0.069	166.739	19205	17091	5978	147	50097
IO1578_33_PC	211	97	7.3	108.6	1.61	0.00	0.446	0.177	0.635	0.064	194.186	23203	20971	6790	165	55060
IO1578_33_PC	221	98	11.5	109.2	1.38	-0.04	0.432	0.182	0.646	0.058	71.576	18509	19548	5510	143	48676
IO1578_33_PC	243	99	11.9	124.5	1.48	0.02	0.457	0.166	0.642	0.058	33.487	19440	19992	5401	162	42748
IO1578_33_PC	263	100	13.3	160.2	1.46	0.03	0.442	0.174	0.632	0.071	490.79	18656	20280	5010	159	40693
IO1578_33_PC	282	101	13.8	124.7	1.45	-0.02	0.427	0.173	0.643	0.059	136.384	17418	17920	4595	159	36491
IO1578_33_PC	303	102	9.8	123.2	1.44	0.01	0.451	0.179	0.642	0.063	15.829	18154	20691	5373	144	44943
IO1578_33_PC	322	103	13.8	124.1	1.33	-0.01	0.421	0.180	0.648	0.063	184.99	19227	15288	6060	154	42302
IO1578_33_PC	343	104	12.0	83.9	1.23	-0.05	0.435	0.171	0.658	0.051	121.576	12593	18554	5173	121	50109
IO1578_33_PC	363	105	11.9	140.2	1.56	-0.03	0.406	0.191	0.650	0.058	225.729	19575	14084	6029	142	48203
IO1578_33_PC	370	106	14.3	142.6	1.64	-0.11	NaN	NaN	NaN	NaN	172.559	22434	16037	7314	163	57602
IO1578_33_PC	390	107	6.6	121.9	1.69	0.01	NaN	NaN	NaN	NaN	189.167	24167	17136	8074	155	67996
IO1578_33_PC	410	108	12.4	185.5	1.85	-0.04	NaN	NaN	NaN	NaN	360.311	26192	16729	8365	186	60208
IO1578_33_PC	430	109	11.8	181.8	1.72	-0.05	NaN	NaN	NaN	NaN	255.033	22357	15294	7278	154	57521
IO1578_33_PC	450	110	8.2	162.4	1.88	-0.02	NaN	NaN	NaN	NaN	357.931	27608	16598	8374	172	67158
IO1578_33_PC	470	111	8.3	162.4	1.77	0.04	NaN	NaN	NaN	NaN	408.912	24663	18387	6497	175	52087
IO1578_33_PC	490	112	7.1	121.9	1.58	0.02	NaN	NaN	NaN	NaN	89.304	29431	20322	7839	169	66726
IO1578_33_PC	510	113	11.4	274.7	1.96	0.04	NaN	NaN	NaN	NaN	NaN	23867	17859	7065	166	56704
IO1578_38_PC	12	114	115.3	796.1	1.04	-0.35	0.450	0.169	0.567	0.067	373.662	26360	12762	4618	176	35619
IO1578_38_PC	21	115	118.4	687.5	1.89	-0.62	0.427	0.160	0.589	0.072	341.991	24317	12290	5304	212	38515
IO1578_38_PC	31	116	7.2	241.0	1.93	0.21	0.451	0.170	0.585	0.074	47.043	22733	17643	5844	220	42269
IO1578_38_PC	41	117	4.9	108.4	1.55	0.04	0.438	0.177	0.605	0.065	45.919	19714	19302	5678	140	46139
IO1578_38_PC	51	118	5.3	95.5	1.54	0.00	0.379	0.185	0.605	0.065	27.802	16431	19452	4756	102	47771
IO1578_38_PC	61	119	5.3	108.2	1.56	0.03	0.413	0.181	0.612	0.055	NaN	22103	23520	5839	132	51460
IO1578_38_PC	71	120	6.7	162.2	1.76	0.12	0.428	0.173	0.631	0.051	NaN	50887	23142	5618	164	49305
IO1578_38_PC	81	121	9.9	157.4	1.73	-0.03	0.423	0.178	0.619	0.061	138.3	38813	17900	4546	214	36147
IO1578_38_PC	91	122	11.0	185.1	1.91	0.02	0.401	0.190	0.637	0.051	NaN	53286	20235	5853	218	42599
IO1578_38_PC	101	123	6.5	181.8	1.83	0.08	0.412	0.184	0.629	0.054	175.207	25316	18272	6752	192	47807
IO1578_38_PC	111	124	6.8	121.9	1.69	0.00	0.410	0.183	0.627	0.060	161.452	30869	18938	6075	170	45280
IO1578_38_PC	121	125	14.0	140.8	1.62	-0.14	0.450	0.169	0.620	0.058	170.847	50394	18741	5144	142	42007
IO1578_38_PC	131	126	54.7	187.1	1.75	-0.52	0.424	0.170	0.609	0.060	151.863	40192	17754	5963	217	44984
IO1578_38_PC	141	127	9.6	211.0	1.92	0.10	0.409	0.188	0.640	0.052	150.933	42435	18465	5796	172	44273
IO1578_38_PC	151	128	9.4	271.0	1.99	0.12	0.425	0.174	0.619	0.067	162.243	20065	17520	4527	166	36725
IO1578_38_PC	161	129	7.5	183.8	1.99	0.14	0.403	0.179	0.634	0.048	159.86	25094	26644	7165	211	55352
IO1578_38_PC	171	130	20.6	124.9	1.75	-0.32	0.420	0.189	0.648	0.041	155.898	17323	13973	4447	117	33952
IO1578_35_PC	10	131	6.6	122.7	1.66	0.04	0.460	0.189	0.650	0.043	35.139	15524	16015	4361	133	46680
IO1578_35_PC	30	132	9.6	160.2	1.99	0.10	0.407	0.179	0.634	0.040	17.214	18848	13576	4977	164	41613
IO1578_35_PC	50	133	7.0	160.2	1.91	0.15	0.396	0.194	0.638	0.042	19.796	29621	20015	7684	183	59091
IO1578_35_PC	65	134	35.5	163.2	1.91	-0.47	0.411	0.186	0.639	0.040	287.958	30206	14176	7539	237	49063
IO1578_35_PC	110	135	21.2	161.7	1.92	-0.30	0.413	0.188	0.636	0.046	62.915	30178	14034	7663	235	49752
IO1578_35_PC	145	136	24.1	125.3	1.74	-0.35	0.389	0.185	0.651	0.032	329.563	31170	12463	6681	235	41885
IO1578_35_PC	210	137	47.7	163.1	1.16	-0.37	0.404	0.180	0.637	0.039	106.565	34195	13727	8057	223	45796
IO1578_35_PC	238	138	31.3	125.3	1.58	-0.43	0.392	0.186	0.645	0.037	112.05	26458	11454	5918	177	41737
IO1578_35_PC	288	139	24.4	125.2	1.92	-0.40	0.399	0.175	0.639	0.042	119.721	29940	12656	6778	187	45417
IO1578_35_PC	308	140	22.8	163.2	2.04	-0.27	0.388	0.188	0.642	0.045	132.549	39712	14668	8329	239	49524
IO1578_35_PC	368	141	18.1	125.0	2.10	-0.36	0.410	0.185	0.647	0.043	386.501	39787	16754	9100	240	58770
IO1578_35_PC	413	142	15.0	241.5	2.33	-0.07	0.411	0.180	0.636	0.050	100.276	27345	18533	7636	180	48474
IO1578_35_PC	428	143	17.1	125.2												

IO1578_35_PC	780	154	40.8	163.3	1.75	-0.51	0.404	0.187	0.637	0.042	250.069	47269	18979	8541	223	51952
IO1578_35_PC	810	155	19.1	162.2	2.17	-0.32	0.393	0.190	0.653	0.033	325.261	21004	11695	5103	137	41300
IO1578_35_PC	860	156	23.2	141.8	1.82	-0.36	0.384	0.194	0.647	0.037	382	27947	13532	6871	165	50590
IO1578_35_PC	899	157	43.5	162.8	1.40	-0.44	0.414	0.189	0.639	0.042	270.635	32134	12397	6609	190	37257
IO1578_35_PC	907	158	26.4	157.4	1.80	-0.40	0.418	0.168	0.639	0.043	382.79	29918	15273	7707	198	49778
IO1578_35_PC	941	159	7.6	123.9	1.81	0.02	0.422	0.195	NaN	0.045	269.176	28817	16389	7958	193	50442
IO1578_35_PC	971	160	5.9	123.6	1.81	0.10	0.406	0.188	0.638	0.047	218.189	29196	17278	8052	183	58544
IO1578_35_PC	1015	161	7.8	108.2	1.73	0.01	0.046	0.173	0.639	0.046	56.893	17931	14511	5209	116	49527
IO1578_35_PC	1028	162	7.6	184.3	2.01	0.09	0.406	0.173	0.639	0.044	106.829	13005	8858	3673	133	29385
IO1578_35_PC	1058	163	14.5	162.0	1.84	-0.11	0.423	0.178	0.642	0.045	NaN	12198	8639	3521	122	26473
IO1578_35_PC	1080	164	12.4	179.9	1.91	-0.07	0.420	0.197	0.639	0.045	205.429	19790	18934	6178	153	46747
IO1578_35_PC	1107	165	24.0	160.8	1.80	-0.60	0.430	0.183	0.636	0.044	56.902	19513	15905	6083	133	48044
IO1578_35_PC	1138	166	4.8	107.9	1.72	0.12	0.425	0.185	0.636	0.046	NaN	18985	15757	5865	123	55396
ELT37_15_P_C	0	167	11.3	162.4	1.70	-0.02	0.420	0.174	0.633	0.057	2.25	25254	18068	2396	173	24304
ELT37_15_P_C	10	168	14.1	162.7	1.72	-0.07	0.391	0.192	0.638	0.047	26.52	30561	15799	2036	166	20144
ELT37_15_P_C	20	169	7.7	107.4	1.47	-0.08	0.403	0.190	0.625	0.070	23.54	26998	19246	2363	158	23496
ELT37_15_P_C	30	170	22.5	162.4	1.70	-0.23	0.400	0.190	0.634	0.047	110.51	86738	16059	2087	191	17579
ELT37_15_P_C	50	171	19.3	125.1	1.68	-0.22	0.421	0.188	0.649	0.043	116.06	43085	21738	2812	276	25774
ELT37_15_P_C	60	172	29.3	162.7	1.73	-0.36	0.395	0.194	0.642	0.037	115.73	89619	18870	2527	235	21479
ELT37_15_P_C	70	173	22.7	183.8	1.69	-0.22	0.404	0.195	0.642	0.054	146.21	117339	15172	1827	360	17206
ELT37_15_P_C	79	174	16.6	124.9	1.52	-0.13	0.432	0.190	0.648	0.044	NaN	91957	18449	2312	231	21224
ELT37_15_P_C	90	175	7.0	120.6	1.29	0.05	0.423	0.197	0.646	0.049	178.29	7540	16546	2091	110	21881
ELT37_15_P_C	100	176	7.7	120.6	1.24	0.06	0.463	0.193	0.640	0.050	191.25	8157	14994	2183	119	24105
ELT37_15_P_C	110	177	8.5	122.7	1.30	0.07	0.439	0.197	0.643	0.050	230.73	6726	15815	2361	108	28500
ELT37_15_P_C	120	178	10.8	121.9	1.26	-0.04	0.429	0.201	0.654	0.034	126.05	9354	21898	3295	136	37468
ELT37_15_P_C	130	179	6.1	120.6	1.24	-0.01	0.445	0.190	0.642	0.055	94.63	5756	14413	2175	106	22836
ELT37_15_P_C	140	180	8.1	122.7	1.30	0.08	0.459	0.191	0.636	0.067	103.17	6218	14279	2113	110	21617
ELT37_15_P_C	150	181	15.5	124.6	1.65	-0.16	0.421	0.192	0.644	0.055	127.43	64213	19575	2508	221	22844
ELT37_15_P_C	160	182	18.5	108.2	1.32	-0.24	0.450	0.198	0.653	0.042	185.36	6530	14983	2307	106	22926
ELT37_15_P_C	170	183	13.2	109.0	1.42	-0.11	0.395	0.195	0.643	0.051	188.67	9886	16641	1978	134	22187
ELT37_15_P_C	180	184	15.7	107.9	1.25	-0.17	0.407	0.199	0.652	0.044	184.38	6735	17468	2184	122	26272
ELT37_15_P_C	190	185	12.4	107.4	1.24	-0.09	0.421	0.206	0.643	0.068	175.78	4897	11340	1847	95	18826
ELT37_15_P_C	200	186	17.9	106.7	1.26	-0.23	0.400	0.202	0.656	0.044	199.45	4888	12167	2022	84	20645
ELT37_15_P_C	210	187	18.9	108.6	1.30	-0.24	0.397	0.199	0.653	0.046	155.28	7933	19573	3278	115	34010
ELT37_15_P_C	220	188	8.0	82.8	1.19	0.05	0.395	0.214	0.653	0.042	138.48	4390	15699	1796	95	18452
ELT37_15_P_C	230	189	15.7	109.3	1.23	-0.14	0.399	0.204	0.653	0.051	108.92	4541	14716	1930	95	26117
ELT37_15_P_C	240	190	15.5	123.2	1.35	-0.11	0.422	0.206	0.651	0.043	61.24	5526	15052	2059	110	23588
ELT37_15_P_C	250	191	NaN	NaN	NaN	NaN	0.435	0.186	0.655	0.047	8.93	5008	13324	2007	100	22786
ELT37_15_P_C	260	192	NaN	NaN	NaN	NaN	0.469	0.169	0.643	0.060	14.88	4856	11648	1550	100	18023
ELT37_15_P_C	270	193	NaN	NaN	NaN	NaN	0.460	0.194	0.643	0.062	14.55	5179	13016	1881	97	21498
ELT37_15_P_C	280	194	NaN	NaN	NaN	NaN	0.457	0.193	0.640	0.059	24.8	7038	16707	2186	121	24920
ELT37_11_P_C	0	195	18.8	162.7	1.69	-0.11	0.396	0.172	0.640	0.047	NaN	24890	18599	2807	231	24325
ELT37_11_P_C	10	196	25.3	162.5	1.65	-0.26	0.387	0.193	0.645	0.047	NaN	9948	18730	2679	227	21833
ELT37_11_P_C	20	197	35.6	186.2	1.67	-0.36	0.394	0.195	0.638	0.047	NaN	9374	17655	2292	245	21170
ELT37_11_P_C	30	198	32.8	125.2	1.23	-0.33	0.380	0.200	0.649	0.034	NaN	9470	14877	1956	259	14871
ELT37_11_P_C	40	199	50.9	163.2	1.03	-0.35	0.404	0.206	0.646	0.037	NaN	10522	16570	1842	261	16935
ELT37_11_P_C	50	200	8.1	123.9	1.72	0.00	0.401	0.197	0.649	0.036	NaN	7219	15215	1901	133	20457
ELT37_11_P_C	60	201	27.0	125.3	1.57	-0.32	0.394	0.187	0.641	0.046	NaN	13239	18659	2518	300	19635

C																			
ELT37_11_P_C	70	202	24.9	125.0	1.58	-0.32	0.412	0.195	0.643	0.048	NaN	10626	19139	2237	242	19682			
ELT37_11_P_C	80	203	19.4	125.2	1.74	-0.22	0.418	0.183	0.635	0.052	NaN	11645	21842	3100	211	29476			
ELT37_11_P_C	90	204	29.6	125.3	1.47	-0.34	0.388	0.198	0.650	0.037	NaN	11650	18346	2159	337	20262			
ELT37_11_P_C	100	205	57.8	162.0	0.69	-0.22	0.414	0.192	0.635	0.052	NaN	14734	16633	2170	394	19887			
ELT37_11_P_C	110	206	33.7	125.2	1.27	-0.36	0.391	0.192	0.649	0.038	NaN	9968	14458	1649	207	14519			
ELT37_11_P_C	120	207	40.0	184.7	1.36	-0.36	0.404	0.214	0.647	0.042	NaN	46805	15413	2168	284	15835			
ELT37_11_P_C	130	208	36.4	186.1	1.54	-0.34	0.393	0.184	0.643	0.041	NaN	71427	14046	1938	209	16241			
ELT37_11_P_C	140	209	48.6	274.7	1.60	-0.40	0.412	0.189	0.640	0.048	NaN	13964	16903	2182	263	19887			
ELT37_11_P_C	150	210	29.3	159.1	1.71	-0.37	NaN	0.195	0.641	0.059	NaN	12283	18305	2187	236	23707			
ELT37_11_P_C	160	211	25.4	125.2	1.60	-0.32	0.420	0.198	0.644	0.046	NaN	12567	16663	2353	285	22624			
ELT37_11_P_C	170	212	36.7	125.2	1.14	-0.34	0.417	0.194	0.638	0.050	NaN	14028	17605	2163	299	20728			
ELT37_11_P_C	180	213	31.0	121.9	1.05	-0.30	0.397	0.201	0.651	0.043	NaN	11534	16289	1702	257	16381			
ELT37_11_P_C	190	214	45.1	162.2	1.09	-0.36	0.387	0.183	0.641	0.043	NaN	11937	18449	1857	265	18052			
ELT37_11_P_C	200	215	36.9	163.1	1.57	-0.40	0.387	0.190	0.638	0.040	NaN	10983	17634	2011	254	20532			
ELT37_11_P_C	210	216	31.4	125.4	1.59	-0.40	0.406	0.194	0.640	0.041	NaN	11551	17196	2079	283	19482			
ELT37_11_P_C	220	217	25.4	125.3	1.65	-0.31	0.357	0.190	0.651	0.042	NaN	9916	15053	1872	208	20127			
ELT37_11_P_C	230	218	18.1	185.7	1.88	-0.09	0.394	0.187	0.644	0.042	NaN	9775	15875	2085	216	21360			
ELT37_11_P_C	240	219	22.3	125.0	1.38	-0.19	0.403	0.190	0.641	0.043	NaN	11974	17885	2399	231	23044			
ELT37_11_P_C	250	220	13.1	108.6	1.32	-0.06	0.396	0.195	0.648	0.042	NaN	7988	16244	2014	263	15930			
ELT37_11_P_C	260	221	16.7	124.6	1.47	-0.13	0.377	0.191	0.648	0.045	NaN	7240	14151	1651	244	12288			
ELT37_11_P_C	270	222	9.1	139.3	1.57	0.03	0.407	0.185	0.648	0.040	NaN	7767	16050	2376	216	21333			
ELT37_11_P_C	280	223	8.5	82.8	1.41	-0.07	0.382	0.188	0.652	0.043	NaN	8788	21536	3249	197	33458			
ELT37_11_P_C	290	224	6.4	92.6	1.34	-0.07	0.398	0.174	0.648	0.039	NaN	7840	25418	3523	169	41047			
ELT37_11_P_C	300	225	6.5	70.9	1.22	-0.06	0.398	0.183	0.648	0.045	NaN	6712	28668	3837	169	46219			
ELT37_11_P_C	310	226	10.0	82.8	1.26	-0.09	0.380	0.186	0.649	0.039	NaN	6791	30234	3639	162	44762			
ELT37_11_P_C	320	227	7.1	82.8	1.38	-0.08	0.388	0.195	0.650	0.040	NaN	6277	19955	2763	127	35804			
ELT37_11_P_C	330	228	9.6	83.7	1.42	-0.11	0.364	0.205	0.650	0.038	NaN	5898	23176	3326	138	38166			
ELT37_11_P_C	340	229	16.1	106.7	1.11	-0.19	0.360	0.199	0.650	0.042	NaN	9428	24953	3415	156	34824			
ELT37_11_P_C	350	230	15.0	355.9	1.97	0.14	0.392	0.176	0.649	0.044	NaN	9196	17729	2569	175	18918			
ELT37_11_P_C	360	231	14.0	234.7	1.81	0.05	0.370	0.195	0.642	0.046	NaN	9173	21142	3282	188	28416			
ELT37_11_P_C	370	232	16.3	120.6	1.45	-0.15	0.382	0.198	0.647	0.044	NaN	9959	19772	3128	222	28540			
ELT37_11_P_C	380	233	21.1	108.9	1.23	-0.23	0.374	0.192	0.646	0.047	NaN	6400	20058	2735	198	23787			
ELT37_11_P_C	390	234	21.11	60.23	0.90	-0.73	0.366	0.192	0.655	0.034	NaN	7136	17985	1890	231	19776			